UNIVERSITÀ DEGLI STUDI DI PADOVA

Dipartimento di Fisica e Astronomia "Galileo Galilei"

Corso di Laurea Magistrale in Fisica

Tesi di Laurea

A novel technique for laser mode-matching in gravitational wave detectors

Relatore

Prof. Giacomo Ciani

Correlatore

Dr. Marco Bazzan

Laureando

Matteo Carlassara

Anno Accademico 2019/2020

UNIVERSITÀ DEGLI STUDI DI PADOVA

Dipartimento di Fisica e Astronomia "Galileo Galilei"

Corso di Laurea Magistrale in Fisica

Tesi di Laurea

A novel technique for laser mode-matching in gravitational wave detectors

Relatore

Prof. Giacomo Ciani

Correlatore

Dr. Marco Bazzan

Laureando

Matteo Carlassara

Anno Accademico 2019/2020

Contents

1 Introduction

Current interferometric gravitational wave detectors were designed to be limited, in much of their sensitive band, by quantum noise in the form of shot noise (at high frequency) or quantum radiation pressure noise (at low frequency). In the current observation run (O3), a squeezed light source has been used to manipulate quantum noise and surpass the limits imposed by the circulating laser power by injecting non-classical states of the electromagnetic field, called squeezed vacuum states, in the interferometer's dark port. Recent O3 results show that this technique was able to reduce the shot noise contribution to the noise spectral density by about one half. To surpass the so called standard quantum limit across the entire sensitivity band, an even more complex variation of this technique will be implemented, which requires the use of a so called "filter cavity" to reflect the squeezed quantum field and rotate the squeezing angle as a function of frequency. The performance of this techniques is however severely limited by light losses. One big contributor to optical losses is the mismatch between the squeezed vacuum beam, the beam circulating into the interferometer and, in the near future, the filter cavity fundamental transverse spatial mode. To be able to monitor and actively correct mode mismatch, an accurate, online sensing technique is needed. A possible solution consists in the introduction of an Electro-Optic Lens (EOL) that can induce radio-frequency sidebands in the Laguerre-Gauss 10 (LG10) transverse mode of the beam. If the modulation frequency is tuned in a way that one sideband is at the cavity LG10 frequency, then the resonance breaks the symmetry of the two sidebands and converts phase modulation into amplitude modulation, making it possible to retrieve an error signal directly from the cavity reflected electric field with the same single-element photodetector used for the Pound Drever Hall (PDH) locking technique. This error signal carries information about the magnitude and nature of the mismatch, providing all is needed to inform a dedicated feedback loop with a suitable actuator to maintain the mismatch at or below the 1% level. The goal of this thesis is to demonstrate the technique on a dedicated bench-top experiment employing an EOL prototype device. The EOL alignment and working point, as well as the cavity lock parameters were optimized in an already existing setup. Simulations and theoretical calculations of the cavity reflected field were performed to evaluate the system non-idealities: both Electro-Optic Modulator (for PDH technique) and EOL modulations effects and interactions, as well as some system imperfections were considered. The simulations confirm that this technique requires a stable cavity lock condition, and for this reason an accurate study and optimization of the feedback loop parameters was done. In conclusion, a characterization of the EOL error signal response to different mismatch conditions are presented.

2 An introduction to laser beam, optical resonator and mode-matching

In this chapter, is given a simple presentation of all the prerequisites needed to analyse this mode matching sensing technique. Focus will be on the notation used for Gaussian beams, optical resonators and mode-matching. In second place, it will be described the Electro-Optic Modulations with Pokels effect and modulation/demodulation process for the Pound Drever Hall (PDH) technique for locking the laser beam to the cavity resonant frequency.

2.1 Gaussian beams

In the context of paraxial waves, a Gaussian beam is described as a solution of the paraxial Helmholtz equation. This Gaussian complex amplitude solution could be obtained directly from the paraboloid wave equation, with a shift of its center by a purely imaginary number iz_R [1] in which z_R is real and it is known as Rayleigh range. The complex amplitude could be expressed as eq. (2.1.1) by the separation of the complex and real exponents in $w(z)$ and $R(z)$ from the complex beam parameter $q(z) = z + iz_R$.

$$U(r,z) = \frac{A_0}{iz_R}\frac{w_0}{w(z)}exp- \frac{r^2}{w(z)}exp-i\left(kz + k\frac{r^2}{2R(z)} - \psi_G(z)\right) \tag{2.1.1}$$

The beam width measured at the z position of the optical axis is described as

$$w(z) = w_0\sqrt{1 + (z/z_R)^2} \tag{2.1.2}$$

with w_0 as the beam waist and

$$z_R = \frac{\pi w_0}{\lambda} = \frac{kw_0^2}{2} \tag{2.1.3}$$

the Rayleigh range as presented before. Another parameter in equation (2.1.5) is the wavefront radius of curvature

$$R(z) = z\left(1 + \left(\frac{z_R}{z}\right)^2\right). \tag{2.1.4}$$

and the last phase term in the equation is known as the Gouy phase $\psi_G(z) = \arctan\left(\frac{z}{z_R}\right)$. It describes the accumulated phase retard of this paraxial wave in comparison with a plan wave (Gouy effect) [1].

The Gaussian beam (or transverse electromagnetic mode TEM_{00}) is only one of the solution of the paraxial Helmholtz equation. A more general and complete orthogonal set of these paraboloidal wavefront solutions are the Hermite-Gaussian (HG) beams or modes of an optical resonator. They include beams with non-Gaussian intensity distribution, but all have the property to match the curvature of spherical mirrors. All the other sets of solutions could be defined as a composition of the HG modes; for example, a solution of the paraxial Helmholtz equation in cylindrical coordinates define the Laguerre-Gauss (LG) modes [2]. The normalized expressions of these modes are reported in eq. (2.1.5).

$$U_{p,l}(r,\phi,z) = \frac{A_{p,l}}{w(z)}\left(\frac{\sqrt{2}r}{w(z)}\right)^{|l|}L_p^{|l|}\left(\frac{2r^2}{w^2(z)}\right)e^{-\frac{r^2}{w^2(z)}-\frac{ikr^2}{2R(z)}-ikz-l\phi-(N+1)\arctan\left(\frac{z}{z_R}\right)} \qquad (2.1.5)$$

with $N = (|l|+2p)$ and the normalization factor $A_{p,l} = \sqrt{\frac{2p!}{\pi(|l|+p)!}}$.

In order to simplify the notation of the equation shown in the next sections, each higher order mode is described as a function of the LG_{00} mode. This was done in order to accentuate the different Guoy phase and coefficients of each mode, as shown in Table 2.1.

$LG_{p,|l|}$	$A_{l,p}$	$L_p^{|l|}$	N+1	$U_{p,l}(r,\phi,z)$
LG_{00}	$\sqrt{2/\pi}$	1	1	$\sqrt{\frac{2}{\pi}}\frac{1}{w(r)}e^{-\frac{r^2}{w(r)^2}-i\frac{z_Rr^2z}{w_0^2(z^2+z_R^2)}+i\arctan(\frac{z}{z_R})}$
LG_{10}	$\sqrt{2/\pi}$	$\left(1-\frac{2r^2}{w(r)^2}\right)$	3	$\left(1-\frac{2r^2}{w(r)^2}\right)e^{2i\arctan(\frac{z}{z_R})}U_{00}(r,\phi,z)$
LG_{01}	$\sqrt{2/\pi}$	1	2	$\frac{\sqrt{2}r}{w(r)}e^{-i\phi+i\arctan(\frac{z}{z_R})}U_{00}(r,\phi,z)$
LG_{11}	$\sqrt{1/\pi}$	$\left(2-\frac{2r^2}{w(r)^2}\right)$	4	$\frac{\sqrt{2}r}{w(r)}\left(2-\frac{2r^2}{w(r)^2}\right)e^{-i\phi+3i\arctan(\frac{z}{z_R})}U_{00}(r,\phi,z)$
LG_{20}	$\sqrt{2/\pi}$	$\left(1-\frac{4r^2}{w(r)^2}+\frac{2r^4}{w(r)^4}\right)$	5	$\left(1-\frac{4r^2}{w(r)^2}+\frac{2r^4}{w(r)^4}\right)e^{4i\arctan(\frac{z}{z_R})}U_{00}(r,\phi,z)$
LG_{02}	$\sqrt{1/\pi}$	1	3	$\frac{\sqrt{2}r^2}{w(r)^2}e^{-2i\phi+2i\arctan(\frac{z}{z_R})}U_{00}(r,\phi,z)$

Table 2.1: List of Laguerre-Gauss modes, polynomials and coefficients

2.2 Optical cavity

An optical cavity (or resonator) is defined as an optical setup with mirrors or optical fibers or crystals, in which the electromagnetic field forms a standing wave at certain frequencies. Gravitational wave detectors uses cavities for different purpose, for example as mode cleaner or filter cavities. Another important application is for the Laser light generation.

The next section gives an introduction to the simplest case of a Fabry-Perot interferometer with two parallel plane mirrors and plane wave light and shortly presents the differences with a triangular cavity.

2.2.1 Fabry-Pérot interferometer

An ideal Fabry-Pérot interferometer is composed by two perfect plane mirrors with no leaks. If a plane wave light interact with the interferometer, then at the surface of the first mirror a portion of the light is directly reflected and the other is transmitted. The same happens at the surface of the second mirror and after a round-trip from these two mirrors, the light field is described by the interference of the light transmitted by the first mirror and the one reflected two times, that covers an optical path length of two times the mutual distance of the 2 mirrors d. If this distance is a multiple of the wavelength,

$$q\lambda = 2d \tag{2.2.1}$$

with q an integer number, then constructive interference can be observed [1, 3].

The standing waves form depends from the boundary conditions of the mirrors set to find a solution of the Helmholtz equation, for example if the solution is set to be equal to zero at the mirrors positions, then the complex amplitude of an arbitrary wave inside the resonator could be described as a sum of interference modes as follow.

$$A(z) = \sum_q C_q \sin\frac{2\pi qz}{\lambda} \tag{2.2.2}$$

Another way to describe the element inside the sine function in this last equation is to consider the phase changing in the electromagnetic field after a cavity round-trip. Each mirror introduces a factor π, so the round-trip phase is 2π and each mode propagates with a different wave number $k = q\pi/d$. In conclusion each in-phase components inside the resonator needed to respect this equality:

$$\phi = 2kd = 2q\pi \tag{2.2.3}$$

The last, but not less important parameter of a resonator is the Free Spectral Range (FSR). It indicates the frequency distance from two consecutive resonant transverse modes. It could be obtained directly from the first consideration (2.2.1).

$$v_{FSR} = \frac{c}{2d} \tag{2.2.4}$$

To describe a real Fabry-Pérot interferometer the non-idealities, as mirrors leaks, needed to be considered. Then the reflected and transmitted fields could be obtained thanks to considerations of the cavity circulating fields [4–6] with the only assumption to consider a stationary input field. To operate with this method, it is be useful to denote the input electric field as E_{IN}, the total transmitted

field as E_t, the total reflected field as E_r and to to give a simplified explanation, inside the resonator only the field transmitted from the first mirror E_i and the circulating field E_c are considered (a complete description can be found here [4]). As a first step, it is useful to describe E_c in terms of E_i inside the cavity.

$$E_c = E_i + r_1 r_2 e^{-i\phi-\beta} E_c \tag{2.2.5}$$

where r_1 and r_2 are the mirrors amplitude reflectivity and β the mean absorption coefficient that characterize the system after a round-trip. A scheme of these fields is reported in Figure 2.1.

The injected field E_i is proportional to the input field with a phase term of $e^{-i\pi/2} = i$ and the first
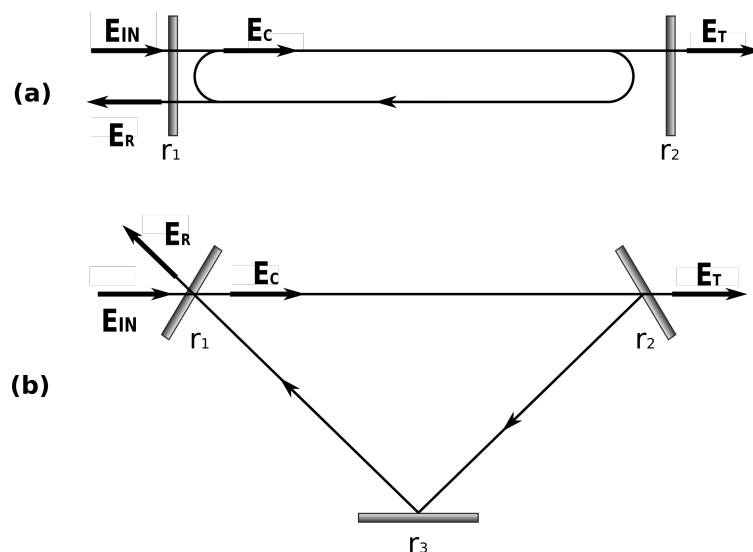

Figure 2.1: Schemes of the circulating fields inside a Fabry-Pérot cavity and a triangular cavity [5]. In the latter, the non collinear setup contribute to astigmatism. Some solutions to remove this aberration consider cavities with spherical mirrors [7].

mirror transmission coefficient: $E_i = it_1 E_{IN}$. With these considerations, the field transmitted after the second mirror is

$$E_t = it_2 e^{-i\phi/2-\beta/2} E_c = \frac{-t_1 t_2 e^{-i\phi/2-\beta/2}}{1 - r_1 r_2 e^{-i\phi-\beta}} E_{IN} \tag{2.2.6}$$

where t_1 and t_2 are the mirror amplitude transmission coefficients. The leaks term is divided by two in this equation because the transmitted light propagates from the first mirror to the second and does not complete a round-trip.

The reflected field results from the composition of the reflected field from the input field and the circulating field transmitted by the first mirror.

$$E_r = r_1 E_{IN} + it_1 r_2 e^{-i\phi-\beta} E_c = r_1 E_{IN} - \frac{-t_1^2 r_2 e^{-i\phi-\beta}}{1 - r_1 r_2 e^{-i\phi-\beta}} E_{IN} \tag{2.2.7}$$

With non perfect optic elements, the reflected field reaches zero only for the cavity resonance frequencies and if $R_1 = R_2 e^{-\beta}$. A resonator with these properties is defined as impedance matched.

Without loss of generality an impedance matched resonator with reflection coefficient $r_1^2 = r_2^2 = R$

was considered for the rest of this chapter. This last part enlightes the base properties of a resonator, as finesse or Q-factor, that characterize the quality of a resonator as a laser "mode cleaner". The Fabry-Pérot frequency transmission intensity response presents a series of Airy distributions, with each center in correspondence of the resonance frequencies. The transmitted intensity is simply the module of the transmitted electric field

$$I_t^2 = \left| \frac{-t_1 t_2 e^{-i\phi/2 - \beta/2}}{1 - r_1 r_2 e^{-i\phi - \beta}} \right|^2 I_{IN}^2 = \frac{1}{1 + (2F/\pi)^2 \sin^2 \phi/2} I_{IN}^2 \tag{2.2.8}$$

where $I_{IN} = |E_{IN}|$ and it is considered a constant for the purpose of this section. The factor $F = \pi\sqrt{R}/(1-R)$ contains all the mirror properties. Theen the reflected intensity is simply obtained from the transmitted intensity as

$$I_r^2 = 1 - \frac{I_t^2}{I_{IN}^2} \tag{2.2.9}$$

and normally from this equation it is estimated the FWHM of the Airy distribution. This condition (2.2.10) needed to be respected at half of the maximum peak intensity.

$$\phi = \frac{2\pi 2d\Delta\nu_{FWHM}}{c} = 2\pi \frac{\Delta\nu_{FWHM}}{\nu_{FSR}} = 2\arcsin\left(\frac{1-R}{2\sqrt{R}}\right) \tag{2.2.10}$$

In classical applications, the mirrors reflection index value is near one, so the arcsin function could be approximate with its argument to obtain a simple and practical equation in order to estimate the resonator finesse coefficient:

$$F = \pi \frac{\nu_{FSR}}{\Delta\nu_{FWHM}} \tag{2.2.11}$$

with respect to the correct finesse equation.

$$\mathcal{F} = \frac{\pi}{\phi} = \frac{\pi}{2\arcsin\left(\frac{1-R}{2\sqrt{R}}\right)} \tag{2.2.12}$$

A resonator with high finesse value is normally achieved with optical elements that limit all possible leaks and reflection coefficients near the ideal value of one. At this point, the separation from consecutive resonances FSR is higher for longer resonator. These conditions are the standard for a "mode cleaner" cavity, in which the resonance frequency components of an input beam are amplified and limited to the cavity line width and all the other components are dampened. But this is still not enough to obtain a stable and clean output because a laser source is characterized by frequency and power instabilities. Normally this problem is solved by controlling the laser parameters with a feedback loop as it will be described at the end of this chapter.

2.2.2 Hermite-Gaussian beams and optical cavities

All the Fabry-Pérot characteristics could be extended to a more general cavity with different number of optical elements. The implementation of spherical mirrors is needed for example if the input beam has a Gaussian profile or it could be described as a sum of HG modes. This solution helps in controlling the laser beam size and evade possible walk-off problems. In the case of multiple mirrors, for example a triangular cavity, it is important to consider that each mirror introduces a phase factor of π in the reflected electric field, so a direct application is for example as a polarization mode cleaner [8]. The side effect is to operate with an astigmatic profile and if required, other strategies need to be considered to limit this aberration.

In presence of a Gaussian input beam, then at least one spherical mirror and a planar mirror are required to implement a stable resonator. This section delineates the requirement of a Gaussian input beam to match a cavity with two spherical mirrors. Then these results are used to describe the characteristic of a stable resonator and some properties of its HG modes.

The first step is to consider the beam radius of eq. (2.1.4) and match its value to the mirror radius of curvatures R_1 and R_2 at the mirror positions in the optical axis z_1 and z_2 and find a suitable value for the beam Rayleigh range [6].

$$\begin{cases} z_1 = z_2 + d \\ R_1 = z_1 + z_R^2/z_1 \\ -R_2 = z_2 + z_R^2/z_2 \end{cases} \tag{2.2.13}$$

After some simple manipulations the Rayleigh range and the mirror positions can be expressed as functions of mirror radii and cavity length.

$$\begin{cases} z_1 = \frac{d(R_2-d)}{R_2+R_1-2d} \\ z_2 = -\frac{d(R_1-d)}{R_2+R_1-2d} \\ z_R = \frac{d(R_1-d)(R_2-d)(R_1+R_2-d)}{R_2+R_1-2d} \end{cases} \tag{2.2.14}$$

Another more compact formulation of these equations is obtained by the introduction of the *cavity g parameters* $g_1 = 1 - d/R_1$ and $g_2 = 1 - d/R_2$. Thanks to the Rayleigh definition in eq. (2.1.3), it is possible to write the beam waist [5] as

$$w_0^2 = \frac{d\lambda}{\pi} \sqrt{\frac{g_1 g_2 (1 - g_1 g_2)}{(g_1 + g_2 - 2g_1 g_2)^2}} \tag{2.2.15}$$

and from eq. (2.1.2) the required beam sizes at positions z_1 and z_2 are

$$w(z_1)^2 = \frac{d\lambda}{\pi} \sqrt{\frac{g_2}{g_1(1-g_1g_2)}} \qquad (2.2.16)$$

$$w(z_2)^2 = \frac{d\lambda}{\pi} \sqrt{\frac{g_1}{g_2(1-g_1g_2)}} \qquad (2.2.17)$$

In conclusion, it is important to notice that these equations have real solutions only for a limited range, known as *range of stability*.
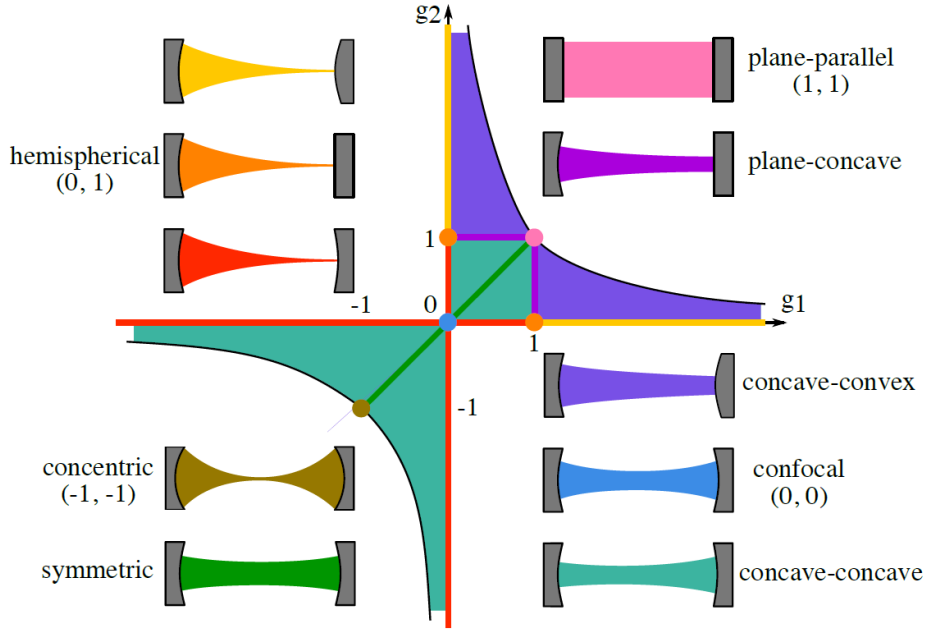
$$0 \le g_1g_2 \le 1 \qquad (2.2.18)$$

Figure 2.2: Range stability representation for Fabry-Pérot interferometers [9].

This inequality is important for two reasons: it limits the possible cavity configurations and at the same time set the Higher Order Modes (HOMs) frequency spacing inside the FSR. As it was introduced in the first section of this chapter, a HG_{nm} mode has the same wavefront, but different amplitude distribution and accumulated round-trip Gouy phase with respect to a Gaussian beam (HG_{00}).

This phase retard depends linearly from the mode numbers n and m (or l and p for LG modes). In general, after a round-trip inside the cavity, each mode fulfill this equation [1]:

$$2kd - 2(n+m+1)(\phi(z_2) - \phi(z_1)) = 2\pi q, \qquad q \in \mathbb{Z} \qquad (2.2.19)$$

Thanks to eq. (2.2.3), (2.2.4) and (2.2.10) is possible to define the wavenumber $k = 2\pi \nu_{q,n,m}/c$

and obtain with some trigonometric identities that

$$\nu_{q,n,m} = (q + (n+m+1)(\pm\sqrt{g_1 g_2}))\nu_{FSR}. \tag{2.2.20}$$

The direct effect of this equation is that HOMs with the same order number $N = n + m = |l| + 2p$ resonates at the same frequency. The index q defines the so called longitudinal or axial modes and their spacing corresponds to ν_{FSR}, the n and m indexes represent different transverse modes and the spacing from two consecutive modes is $\nu_{q,n,m} - \nu_{q,n',m'}$. A particular attention is to be given to even transverse modes in a confocal resonator. In fact for the case of a symmetric resonator and a even m number another shift of $\nu_{FSR}/2$ is introduced.

2.3 Mode-Matching

All the different methods that contribute at the minimization of the inequalities from the cavity expected beam properties and the real input beam are called Mode-Matching technique. Common practical solutions use lenses and other optical elements to shape the input beam to the required size and focus position [5, 10]. The effect of a non optimal matching situation is defined as mismatch. The main consequence of a mismatch is to inject in both lower and higher cavity order modes a portion of the laser beam power. The lower order modes are characterized by lower diffraction losses and leaks, but for the higher order modes the cavity present a weak response due to stronger leaks and diffraction effect.

For the gravitational wave detectors optimization, different LG_{nm} beams had been studied in order to break the standard quantum limit and reduce the mirror thermal noise [11], but for all different cases a fine mode-matching technique is required.

The main misalignments that contribute to mismatch are four and their effects are listened in Table 2.2. The first describes a situation where the input beam axis is shifted from the correct optical axis, but remains parallel to it. The second considers a beam axis with a tilt with respect to the optical axis, but with the correct waist size and position. They can be manually limited by design in the optical path before the cavity a two mirror galvanometer system. The last two misalignments require a more accurate beam shaping. A simple telescope before the cavity can help for this type of mode-matching.

These solutions consists of passive elements and without a feedback loop it is not possible to actively limit mismatch. So, the first step would consider a method to retrieve information of the beam mismatch from the cavity transmitted or reflected fields. To be able to monitor and actively correct mode mismatch, an accurate, online sensing technique is needed. Active solutions for alignment sensing were studied in the last years [12]. Currently different projects are under development to find a reliable on-line sensing technique for mismatch in waist size and position.

D.O.F.	HOM	Phase [deg]
Transverse position	HG_{10}/HG_{01}	0
Angular tilt	HG_{10}/HG_{01}	$\pi/2$
Waist size	LG_{10}	0
Waist position	LG_{10}	$\pi/2$

Table 2.2: Light couplings to HOMs for a non aligned input beam to a two mirror cavity [10]. Each misalignment source coupled with a specific HOM and induce a phase shift.

In this thesis an innovative approach was studied. The tested solution consists in the introduction of an Electro-Optical Lens (EOL) that can induce radio-frequency sidebands in the LG10 transverse mode of the beam. In the next chapter a complete explanation of this technique will be given; this chapter will conclude with the introduction of the last concepts and methods used in this innovative approach. For this reason it will be shortly introduced the Electro-Optic Modulation effect and the Pound Drever Hall (PDH) technique. Before mode-matching, the laser frequency output stabilization and match with the cavity resonant modes are required in general and for gravitational wave detectors too.

2.4 Electro-Optic Modulation

The Electro-Optic Modulation can be achieved only in a specific classes of crystals - that for the presented method is lithium niobate ($LiNbO_3$) - thanks to the Pockels effect. This effect produces a refractive index change in a crystal material when an electric field is applied to it.

Lithium Niobate is an artificial crystal [6, 13] that has a trigonal crystal structure and many other important properties, for example large electro-optic, piezoelectric and photo-elastic coefficients other than being naturally an uni-axial birefringent material. For these reasons it is nowadays a wildly used crystal. This ferroelectric material was synthesized for the first time in 1928 by Zachariasen and its first synthesization as a single crystal was done in the '60 in the Bell Laboratories.

A quantitative description of the EOM effect starts with the introduction of the index ellipsoid that could be written as follow with x, y, z the optical axes and n_x, n_y, n_z the crystal refraction index for different axes [6, 14].

$$\frac{x^2}{n_x^2} + \frac{y^2}{n_y^2} + \frac{z^2}{n_z^2} = 1 \qquad (2.4.1)$$

Without loss of generality it is taken to coincide the crystal z axis with the input laser beam optical axis. Considering the Lithium Niobate crystal orientation in a way that the x and y direction share

the same refraction indexes (called *extraordinary refraction index*) then the z axis index is known as the *ordinary refraction index* and eq. (2.4.1) assumes a bilinear form.

$$\frac{x^2 + y^2}{n_e^2} + \frac{z^2}{n_o^2} = 1 \tag{2.4.2}$$

With a general crystal orientation and with tensor notation, this equation assumes a more compact form

$$\frac{1}{\varepsilon_{ij}} x_i x_j = 1 \tag{2.4.3}$$

where ε_{ij} is a symmetric dielectric tensor for the Lithium Niobate crystal.

If an electric field is applied to the crystal, then the dielectric tensor changes accordingly because it is a function of the charges distributions inside the crystal. The modification is a linear or quadratic function to the applied electric field (or the material polarization). For the Pockels effect, this change has a linear dependence from the electric field

$$\Delta\left(\frac{1}{\varepsilon_{ij}}\right) = r_{ijk} E_k \tag{2.4.4}$$

Where r_{ijk} is the electro-optic tensor. Thanks to the crystal symmetry and the equation $n_{ij}^2 = \varepsilon_{ij}$ then, the modification of the index ellipsoid can be described as

$$\Delta\left(\frac{1}{n_{ij}}\right)^2 = \sum_{ij} r_{ij} E_j. \tag{2.4.5}$$

The electro-optic tensor for a Lithium Niobate crystal is in the 3m symmetry group (more detailed information could be found here [14, 15]) and in conclusion, in the same frame coordinate system described at the beginning of this section, the electro-optic effect generated by an electric field parallel to the z axis E_z modifies the refraction indexes in the crystal as follow:

$$n_x = n_y = n_o(1 - \frac{1}{2} n_o^2 r_{13} E_z) n_z = n_e(1 - \frac{1}{2} n_e^2 r_{33} E_z) \tag{2.4.6}$$

where $r_{13} = 10.0 \, [pm/V]$ and $r_{33} = 32.2 \, [pm/V]$ [15].

The main uses of an Electro Optic Modulator are two: Amplitude Modulation or Phase modulation.

1. **Amplitude Modulation:** this effect consist in a change of the input beam polarization proportional to the voltage applied to the crystal. The maximum effect is achieved when the applied voltage corresponds to the *half-wave voltage* $V_\pi = k n_e^3 r_{33}$ and at it value the crystal induce a retard of π(for example, for an input beam with polarization along x and with crystal axis x' and y', the output beam presents a complete polarization along y' or x'). If the applied voltage has a frequency oscillation, in presence of two polarizers before and after the crystal the output field presents a nearly sinusoidal oscillation from the light

polarisation.

2. **Phase Modulation:** in the case of an input beam which polarization is in one of the ordinary axes of the crystal (for example x') and with an electric field directed for example along z, then a change in an electric field does not change the polarization but introduces a phase shift in the output beam.

In a simple case with a crystal of length d, a plane wave with wave number $k = \frac{2\pi}{\lambda}$ acquires a phase shift of

$$\Delta\alpha = \pi\frac{V_z(t)}{V_\pi} = k\Delta n(t)d. \tag{2.4.7}$$

If the voltage applied to the crystal presents an oscillation with frequency Ω then the phase shift is proportional to $\varepsilon cos(\Omega t)$ and the beam electric field is

$$E_{OUT}^{EOM}(x,t) = E_0 e^{i(kx+\omega t+\varepsilon cos(\Omega t))} + c.c. \tag{2.4.8}$$

Normally, high quality Electro-Optic Modulator (EOM) has a really small modulation index ε and it is considered as a perturbation. In this case the electric field could be approximated with the exponential series expansion and thanks to the Eulero identity it is possible to write the Jacobi-Anger equation:

$$E_{OUT}^{EOM}(x,t) = E(x,t)\left(J_0(\varepsilon) + \sum_{s=1}^{\infty} J_s(\varepsilon)e^{is\Omega t} + \sum_{s=1}^{\infty}(-1)^s J_s(\varepsilon)e^{-is\Omega t}\right) \tag{2.4.9}$$

In the setup proposed for this thesis theare are two Lithium Niobate crystals, the first is used as an Electro-Optic Modulator (EOM) and the second is a custom built Electro-Optic Lens (EOL). The EOM is used for the PDH technique. It modulates the input light at Radio-Frequency with phase modulation to generate the positive and negative sidebands at frequency $\nu_{FSR} \pm \Omega/2\pi$.
The EOL device was built [6] to produce sidebands in LG_{10} mode.

2.5 Pound Drever Hall technique

This technique uses a phase-modulation sidebands to generate an error signal proportional to the frequency difference between a reference optical cavity resonance and an incident laser beame [16]. This technique works both with reflected and transmitted light, in this section is dedicated to a simple introduction of the first described situation. To retrieve an error signal, the laser beam is phase modulated with a EOM at RF. Then a single-element photodetector converts the reflected light to photo-current and demodulates it with the RF signal used for the modulation [17]. A low-pass filter is used to isolate the signal componentes at the modulation frequency . After that, the final error signal is converted in an Actuation Signal by a PID controller to actuate on the laser feedback loop.

This error signal contains a great number of information. For example from its slope near the cavity's resonance it is possible to retrieve information of mismatch [17] and from its offset the Residual Amplitude Modulation induced by the EOM device [18]. Other information could be extrapolated by the photocurrent In-phase and Quadrature-phase (IQ) demodulation. In the following section details of these analysis method are showed.

2.5.1 Error signal and Lock-In

This section describes how the photocurrent is normally elaborated from the electronics in order to obtain the Error signal for the Lock-In and for the IQ analysis. As a first step, thanks to a trans-impedance stage, the photocurrent signal is converted to a voltage signal and its contribution consist in the introduction of a impedance factor R (in the simulation presented in the next chapters, it is considered a constant equal to 1 [V/A]). The demodulated signal is defined as:

$$V(\Omega) = RI_{PD}^{\Omega} \cdot A\cos(\Omega t + \phi) \tag{2.5.1}$$

The phase shift term ϕ is introduced to consider and correct the different phase from the modulation and demodulation signals, or to introduce a phase if needed. In our the setup, the same reflected signal is demodulated with 2 different electronic chains. The first for the PDH technique and the second for the IQ analysis. In the second case, the voltage signal is demodulated with two signals generated by a local oscillator and a power splitter that insert a phase difference of $\pi/2$. These two signal were labelled as V_Q and V_I (The goal is to analyse both terms of eq. (3.1.19) thanks to these signals). In general, the demodulated signal has this form:

$$\begin{aligned}V(\Omega_1) &= AI_1\cos(\Omega_1 t)\cos(\Omega t + \phi) + AI_2\sin(\Omega_1 t)\cos(\Omega t + \phi) = \\ &= \frac{AI_1}{2}\left[\cos((\Omega_1 + \Omega)t + \phi) + \cos((\Omega_1 - \Omega)t - \phi)\right] + \\ &+ \frac{AI_2}{2}\left[\sin((\Omega_1 + \Omega)t + \phi) + \sin((\Omega_1 - \Omega)t - \phi)\right]\end{aligned} \tag{2.5.2}$$

and thanks to the low-pass filter, only terms with the same the local oscillator frequency contribute to the error signal. In the case of $\Omega_1 = \Omega$, after the filter, the error signal has this form:

$$\begin{aligned}V_Q^{\Omega} &= +\frac{AI_1}{2}\cos(\phi) - \frac{AI_2}{2}\sin(\phi) \\ V_I^{\Omega} &= \frac{AI_1}{2}\sin(\phi) + \frac{AI_2}{2}\cos(\phi)\end{aligned} \tag{2.5.3}$$

For the PDH technique only one of them is extracted from the photocurrent.

Normally, the I and Q error signals present a dependence from constant phase terms in ϕ. To remove its contribution from eq. (2.5.3), it is normally studied them module and phase.

In this generic situation, the module is defined as

$$M_{IQ} = \sqrt{V_I^{\Omega 2} + V_Q^{\Omega 2}} = \frac{A}{2}\sqrt{I_1^2 + I_2^2} \tag{2.5.4}$$

3 RF mode sensing technique

The on-line mismatch sensing technique studied in this thesis consists in the introduction of an Electro-Optic Lens (EOL) that can induce RF sidebands in the LG_{10} transverse mode of the laser beam. If the modulation frequency is tuned in a way that one sideband is at the cavity LG10 frequency, then the resonance breaks the symmetry of the two sidebands and converts phase modulation into amplitude modulation, making it possible to retrieve an error signal directly from the cavity reflected electric field with the same single-element photodetector used for the PDH locking technique. This error signal carries information about the magnitude and nature of the mismatch, providing all is needed to inform a dedicated feedback loop with a suitable actuator to maintain the mismatch at or below the 1% level. The electrodes in the EOL device were designed in a way that they can induce in the crystal a lens effect for four times inside the crystal [6] to maximize the polarization effect inside the crystal given the r_{33} value. In this chapter it will be described the theoretical calculation and the simulations of error signals obtained from a detailed study of the cavity reflected field. Then some of the system non-idealities will be evaluated thanks to the simulations: both electro-Optic Modulator (for PDH technique) and EOL modulations effects and interactions, as well as some system imperfections were considered.

3.1 Theory and mismatch calculation

The starting point of the theoretical discussion lies in the mismatch description in term of a Fabry-Pérot stable optical cavity LG eigenmodes. They form a complete set and it is possible to expand a general input beam as a linear combination of these eigenmodes. To simplify the notation and focus on the important part of these expressions, the beam series expansion at the cavity's waist position was developed with the same structure shown by Z. Anderson and P. Fulda [10,12]. The considered input Gaussian beam (TEM_{00}) has a perfect alignment condition and a little perturbation in mode matching (for waist size and position).

3.1.1 Mismatch description with LG modes

Given two different sets of Laguerre-Gauss modes, the first defined in the laser input beam base U_{ij} and the second in the cavity base V_{kl}, in an ideal situation, where the beam and the cavity are perfectly aligned, both sets correspond in a way that: $\int U_{ij}V_{kl}^* = \delta_{ik}\delta_{jl}$. However, if a mismatch

is present, the base-change matrix is not a diagonal matrix anymore and the next two section are
dedicated at its approximated estimation.

The LG modes were considered in their Taylor and McLaurin series up to the second order near
w_0 and $z_0 = 0$. It is important to consider that in both situation, all the the exponential Gouy phase
terms are equally one and their contribution is limited only with their derivative elements. For the
same position, LG_{00}, LG_{10} and LG_{20} modes do not have a dependency from ϕ and it was referred
to them as $U_{l,p}(r, w_0)$ in the below equations.

The first part follows these series expansion in terms of the cavity waist size w_0 and position z_0
and concludes with the change-base matrix characterization.

The second part introduces the EOL modulation effect and the formulation of the cavity's input
beam deformed by EOL in terms of the cavity LG eigenmodes. The third part focuses in the
interaction of the input beam electric field and the cavity and some photocurrent signals were
characterized from starting from different complex reflectivity function $F(\omega)$ conditions. In the
fourth part, the complex reflectivity function contributions were expressed in term of sinusoidal
functions thanks to the composition with the real and imaginary part of the input beam coefficients.
The last part is dedicated to the simulation results in perfect condition and in presence of non-
idealities in the experimental setup.

3.1.2 Waist size mismatch

This section evaluates a mismatch $\beta = \frac{\delta w_0}{w_0^{CAV}} = \frac{w_0^{IN} - w_0^{CAV}}{w_0^{CAV}}$ of the beam waist with respect to the
cavity waist. They are considered to have the same waist position. The first part is dedicated to
the Maclaurin series expansion of the term $U_{00}(r, w_0 + \delta w_0)$ up to the second order perturbation in
mismatch.

$$U_{00}(r, w_0 + \delta w_0) \simeq U_{00}(r, w_0) + \delta w_0 \left.\frac{\partial U_{00}}{\partial w_0}(r, z)\right|_{z=0} + \frac{\delta w_0^2}{2} \left.\frac{\partial^2 U_{00}}{\partial w_0^2}(r, z)\right|_{z=0} =$$

$$= U_{00}(r, w_0) \left[1 - \frac{\delta w_0}{w_0}\left[1 - \frac{2r^2}{w_0^2}\right] + \frac{\delta w_0^2}{w_0^2}\left[1 - \frac{4r^2}{w_0^2} + \frac{2r^4}{w_0^4} - \frac{r^2}{w_0^2}\right]\right] =$$

$$= U_{00}(r, w_0) - \beta U_{10}(r, w_0) + \beta^2 \left[U_{20}(r, w_0) + \frac{1}{2}\left[1 - \frac{2r^2}{w_0^2}\right] U_{00}(r, w_0) - \frac{1}{2}U_{00}(r, w_0)\right]$$

The result is reported in eq. (3.1.1) as a linear composition of LG modes.

$$U_{00}(r, w_0 + \delta w_0) \simeq \left[1 - \frac{\beta^2}{2}\right] U_{00}(r, w_0) + \left[-\beta + \frac{\beta^2}{2}\right] U_{10}(r, w_0) + \beta^2 U_{20}(r, w_0) \qquad (3.1.1)$$

At this point, the same process was repeated for the $U_{10}(r, w_0 + \delta w_0)$ mode and its expansion is reported in the equation below, together with its result in eq. (3.1.2).

$$U_{10}(r, w_0 + \delta w_0) \simeq U_{10}(r, w_0) + \delta w_0 \left. \frac{\partial U_{10}}{\partial w_0}(r, z) \right|_{z=0} =$$

$$= U_{10}(r, w_0) - U_{00}(r, w_0) \left[-\frac{8r^2}{w_0^2} + \frac{4r^4}{W_0^4} + 1 \right] \frac{\delta w_0}{w_0} =$$

$$= U_{10}(r, w_0) - \beta \left[2U_{20}(r, w_0) - U_{00}(r, w_0) \right]$$

$$U_{10}(r, w_0 + \delta w_0) \simeq \beta U_{00}(r, w_0) + U_{10}(r, w_0) - 2\beta U_{20}(r, w_0) \tag{3.1.2}$$

3.1.3 Waist position mismatch

This section evaluates a mismatch $\gamma = \frac{\delta z_0}{2z_R^{CAV}} = \frac{z_0^{IN} - z_0^{CAV}}{2z_R^{CAV}}$ of the beam waist position with respect to the cavity waist position in the optic axis. For the calculation below, without loss of generality, the optical axis origin is considered to coincide with the cavity waist position.

The first part is dedicated to the McLaurin series of the term $U_{00}(r, \delta z_0)$ up to the second order.

$$U_{00}(r, \delta z_0) \simeq U_{00}(r, w_0) + \delta z_0 \left. \frac{\partial U_{00}}{\partial z}(r, z) \right|_{z=0} + \frac{\delta z_0^2}{2} \left. \frac{\partial^2 U_{00}}{\partial z^2}(r, z) \right|_{z=0} =$$

$$= U_{00}(r, w_0) \left[1 + i\frac{\delta z_0}{2z_R} \left[2 - \frac{2r^2}{w_0^2} \right] - \frac{\delta z_0^2}{2z_R^2} \left[-4\frac{r^2}{w_0^2} + 2 + \frac{r^4}{w_0^4} \right] \right] =$$

$$= U_{00}(r, w_0) \left[1 + i\gamma \right] + i\gamma U_{10}(r, w_0) +$$

$$- \gamma^2 U_{00}(r, w_0) \left[\left[1 - 4\frac{r^2}{w_0^2} + \frac{2r^4}{w_0^4} + 2 - 4\frac{r^2}{w_0^2} + 1 \right] \right]$$

$$= U_{00}(r, w_0) \left[1 + i\gamma \right] + i\gamma U_{10}(r, w_0) - \gamma^2 \left[U_{20}(r, w_0) + 2U_{10}(r, w_0) + U_{00}(r, w_0) \right]$$

Reorganizing the different terms, the final equation is:

$$U_{00}(r, \delta z_0) \simeq \quad U_{00}(r, w_0) \left[1 + i\gamma - \gamma^2 \right] + U_{10}(r, w_0) \left[i\gamma - 2\gamma^2 \right] - \gamma^2 U_{20}(r, w_0) \tag{3.1.3}$$

Some of the $U_{10}(r, \delta z_0)$ series calculation are shown below up to the first order

$$U_{10}(r, \delta z_0) \simeq U_{10}(r, w_0) + \delta z_0 \left. \frac{\partial U_{10}}{\partial z}(r, z) \right|_{z=0} =$$

$$= U_{10}(r, w_0) + i\frac{\delta z_0}{z_R} U_{00}(r, w_0) \left[-\frac{r^2}{w_0^2} + 3 \right] \left[1 - \frac{2r^2}{w_0^2} \right] =$$

$$= U_{10}(r, w_0) + i2\gamma \, U_{00}(r, w_0) \left[1 - \frac{4r^2}{w_0^2} + \frac{2r^4}{w_0^4} + \frac{3}{2} \left[1 - \frac{2r^2}{w_0^2} \right] + \frac{1}{2} \right]$$

and it could be rewritten in a easier form as shown in eq. (3.1.4).

$$U_{10}(r, \delta z_0) \simeq i\gamma \, U_{00}(r, w_0) + U_{10}(r, w_0)\left[1 + i3\gamma\right] + i2\gamma U_{20}(r, w_0) \qquad (3.1.4)$$

To define a correct series expansion, the sum of the above equations (3.1.1), (3.1.3), (3.1.2) and (3.1.4) needs to be considered in order to define the change-base matrix. In the next equation the dependence of each LG modes to the beam radius and waist was hidden in order to lift the equations.

$$V_{00} \simeq U_{00}\left[1 + i\gamma - \frac{\beta^2}{2} - \gamma^2\right] + U_{10}\left[i\gamma - \beta + \frac{\beta^2}{2} - 2\gamma^2\right] + U_{20}\left[\beta^2 - \gamma^2\right] \qquad (3.1.5)$$

$$V_{10} \simeq U_{00}\left[i\gamma + \beta\right] + U_{10}\left[1 + i3\gamma\right] + U_{20}\left[i2\gamma - 2\beta\right] \qquad (3.1.6)$$

And the resulting approximated matrix is reported up to the first order in eq. (3.1.6).

$$V = \begin{pmatrix} 1 & 0 \\ 0 & 1 \end{pmatrix} + \begin{pmatrix} i\gamma & i\gamma - \beta \\ i\gamma + \beta & 3i\gamma \end{pmatrix} \qquad (3.1.7)$$

3.1.4 Electro optic actuator

The Electro-Optic lens (EOL) effect is to generate two modulated sidebands at the frequencies $\omega + \Omega$. It operates as a lens and modifies the input beam in both waist size and position of the input beam and this modification could be expressed as [6]:

$$\frac{\delta w_0^{EOL}}{w_0^{IN}} = B = \frac{m_B}{2}\left[e^{i\Omega t} + e^{-i\Omega t}\right]$$
$$\frac{\delta z_0^{EOL}}{2z_R^{IN}} = G = \frac{m_G}{2}\left[e^{i\Omega t} + e^{-i\Omega t}\right] \qquad (3.1.8)$$

These eq. (3.1.8) needed to be applied at the input beam in its own base. Using the first line of the matrix (3.1.6), the beam after EOL is deformed in this way:

$$U_{IN}(r, z) = \left[1 + iG\right]V_{00}(r, z) + \left[iG - B\right]V_{10}(r, z) \qquad (3.1.9)$$

The EOL is at a fixed distance Z from the cavity first mirror and each beam mode propagates with a different Gouy phase in this distance, the phase difference $\Delta\psi = 2arctan\left(Z/z_R\right)$ from the first two modes will be considered in the next steps for this reason. In the cavity base then, the resultant

input complex amplitude could be express as:

$$V_{IN}(r,z) = [1+iG] \cdot [\, [1+i\gamma]\, U_{00}(r,Z) + [i\gamma - \beta]\, U_{10}(r,Z)\,] +$$
$$+ [iG - B]\, [\, U_{00}\, [i\gamma + \beta] + U_{10}\, [1 + i3\gamma] + U_{20}\, [i2\gamma - 2\beta]\,]\, e^{i\Delta\psi} \tag{3.1.10}$$

In general, the Electric field of the input monochromatic beam is given by the product of the complex amplitude by the plane wave term $E_0 e^{i\omega t - ikZ}$:

$$E_{IN}(r,Z) = E_0 e^{i\omega t - ikZ} \left\{ \left[1 + i\gamma - G\left[\gamma\left(1 + e^{i\Delta\psi}\right) - i\left(1 + \beta e^{i\Delta\psi}\right) \right] - B e^{i\Delta\psi} (\beta + i\gamma) \right] U_{00} + \right.$$
$$+ \left[i\gamma - \beta - G\left[\gamma\left(3 e^{i\Delta\psi} + 1\right) - i\left(e^{i\Delta\psi} - \beta\right) \right] - B e^{i\Delta\psi} [1 + 3i\gamma] \right] U_{10} +$$
$$\left. + [iG - B]\, [i2\gamma - 2\beta]\, U_{20} e^{i\Delta\psi} \right\} \tag{3.1.11}$$

where k is the wavenumer and ω is the angular frequency. This field contains all the effects induced by EOL up to the first order.

3.1.5 Cavity reflected field

The complex amplitude of the cavity's reflected field is the convolution of the input cavity field with the cavity complex reflection function $F_{l,p}(\omega)$. Thanks to the convolution theorem, in the Fourier transform space, the convolution becomes the simple product of the transformed term. The key is to use the orthogonality of the cavity base $\{U_{l,p}\}$ to study the coefficient of each modes independently.

$$u_{00} = c_{00} F_{00}(\omega) e^{i\omega t} - d_{00} \left[e^{it(\omega + \Omega)} F_{00}(\omega + \Omega) + e^{it(\omega - \Omega)} F_{00}(\omega - \Omega) \right]$$
$$u_{10} = -c_{10} F_{10}(\omega) e^{i\omega t} - d_{10} \left[e^{it(\omega + \Omega)} F_{10}(\omega + \Omega) + e^{it(\omega - \Omega)} F_{10}(\omega - \Omega) \right] \tag{3.1.12}$$

The coefficients contain the information regarding the input beam.

$$c_{00} = 1 + i\gamma$$
$$d_{00} = \frac{m_G}{2}\left[\gamma\left(1 + e^{i\Delta\psi}\right) - i\left(1 + \beta e^{i\Delta\psi}\right) \right] + \frac{m_B}{2} e^{i\Delta\psi} (\beta + i\gamma)$$
$$c_{10} = \beta - i\gamma$$
$$d_{10} = \frac{m_G}{2}\left[\gamma\left(3 e^{i\Delta\psi} + 1\right) - i\left(e^{i\Delta\psi} - \beta\right) \right] + \frac{m_B}{2} e^{i\Delta\psi} [1 + 3i\gamma] \tag{3.1.13}$$

The photocurrent read from the single-element Photodiode (PD) is proportional to the squared module of the reflected field, integrated in all the plane orthogonal to the optical axis at the PD

coordinates:

$$I_{PD} \propto \iint E_{refl}E^*_{refl}dxdy \tag{3.1.14}$$

Another important consideration that has to be done is that it is possible to directly integrate the FFT modules of the LG modes thanks to the Parseval Theorem.

With all these consideration, the integral can be written in this way:

$$I_{PD}(t) = \frac{1}{\sqrt{2\pi}} \int_{-\infty}^{+\infty} d\omega \left[|u_{00}(\omega)|^2 \iint |E_0 U_{00}|^2 dxdy + |u_{10}(\omega)|^2 \iint |E_0 U_{10}|^2 dxdy \right] e^{-i\omega t} \tag{3.1.15}$$

where E_0 is considered as a constant complex number and its intensity is $I_0 = E_0 \cdot E^*_0$. It is then important to remember that the photocurrent is multiplied with a demodulated signal at frequency Ω and low-pass filtered. For this reason, in this section, only terms with coefficient $e^{\pm i\Omega t}$ will be contemplated. Considering that the LG modes described in eq. (2.1.5) are normalised functions, then eq. (3.1.15) simplifies as follow:

$$
\begin{aligned}
\frac{I_{PD}}{I_0}(\omega) =& |u_{00}|^2 + |u_{10}|^2 = \\
& - c_{00}F_{00}(\omega)d^*_{00} \left(F^*_{00}(\omega+\Omega)e^{-i\Omega t} + F^*_{00}(\omega-\Omega)e^{i\Omega t} \right) - c.c. + \\
& + c_{10}F_{10}(\omega)d^*_{10} \left(F^*_{10}(\omega+\Omega)e^{-i\Omega t} + F^*_{10}(\omega-\Omega)e^{i\Omega t} \right) + c.c. + ...
\end{aligned} \tag{3.1.16}
$$

The next considerations was done only with terms up until the first order in γ and β and with this approximation the product coefficients can be written as follow:

$$
\begin{aligned}
c_{00}d^*_{00} &= \left(i + \gamma e^{-i\Delta\psi} + i\beta e^{-i\Delta\psi} \right) \frac{m_G}{2} + (\beta - i\gamma) e^{-i\Delta\psi} \frac{m_B}{2} \\
c_{10}d^*_{10} &= \frac{e^{-i\Delta\psi}}{2} \left(\gamma m_G + \beta m_B + i\beta m_G - i\gamma m_B \right)
\end{aligned} \tag{3.1.17}
$$

To achieve a situation where the induced photocurrent is zero, in a first order approximation, the conditions $F_{00}(\omega+\Omega) = F^*_{00}(\omega-\Omega)$ and $F_{00}(\omega) = F^*_{00}(\omega)$ need to be satisfied. For example this situation is achieved when the laser Carrier is on resonance with the cavity LG_{00} mode and the sidebands are on resonance with high order modes with the same reflection coefficient $F_{10}(\omega+\Omega) = F^*_{10}(\omega-\Omega)$ (in this case the the reflection coefficient is totally real and equal to zero). In a general situation, in which these three condition are preserved, the photocurrent terms at frequency Ω are:

$$
\begin{aligned}
\frac{I^\Omega_{PD}(\omega)}{4I_0 \cos(\Omega t)} =& \left[-\cos(\Delta\psi)(\gamma m_G + \beta m_B) - \sin(\Delta\psi)(\gamma m_B - \beta m_G) \right] F^*_{00}(\omega)F_{00}(\omega+\Omega) + \\
& + \left[\cos(\Delta\psi)(\gamma m_G + \beta m_B) - \sin(\Delta\psi)(\gamma m_B - \beta m_G) \right] F^*_{10}(\omega)F_{10}(\omega+\Omega)
\end{aligned} \tag{3.1.18}
$$

The phase difference $\Delta\psi$ is dependent from the distance Z of the EOL to the cavity. In optimal condition it would be more advisable to match the Z distance in a way that $\Delta\psi = q2\pi$. In an optical

table it is not possible to exactly measure Z, so a easy way to compensate its contribution in the error signal is to tune the phase in eq. 2.5.1. In the perfect situation, where the optimal Z value is matched, the current could reach zero in eq.(3.1.18) only if the Carrier and the sidebands are on resonance with the cavity modes (or if there is no input beam).

If the laser frequency ω is maintained on resonance with the cavity (thanks to the PDH technique), then the complex reflection function is zero for all resonant components, as said before. This situation could be helpful because the first 2 conditions are a given ($F_{00}(\omega) = 0$ and $F_{10}(\omega) = F_{00}(\omega + \Omega) = 1$). However, in order to retrieve a photocurrent signal that it is dependant only from the mismatch, a condition needed to be satisfied for the $F_{10}(\omega \pm \Omega)$ components. The symmetric situations were analysed in the last paragraph, now an example of an asymmetric situation will be enlighted. For example, a situation where $F_{10}(\omega + \Omega) = 0$ and $F_{10}(\omega - \Omega) = 1$ and the positive sideband is on resonant with the U_{10} mode, while the negative one is far from a resonant frequency. This is the wanted condition described for the mode match sensing method. Now, eq. (3.1.16) could be written as:

$$\frac{I_{PD}^{\Omega}}{I_0} = (\gamma m_G + \beta m_B) \cos(\Omega t - \Delta \psi) + (\beta m_G - \gamma m_B) \sin(\Omega t - \Delta \psi) \tag{3.1.19}$$

3.1.6 Error signal analysis

The error signals of interests are three, as was said: the error signal for the PDH technique and the I and Q signals. The calculation presented in this section are valid for all of them and a detailed explanation with a simulation up to the second order will follow in the next chapter in the section EOM and sideband couplings.

In eq. (3.1.15) all the dependencies from the laser frequency are contained the Complex Reflection Function (CRF) for the LG modes as

$$F_{pl}(\omega) = \frac{r_1 - r_2 \left(r_1^2 + t_1^2 \right) e^{-i\left(\frac{\omega}{\Delta \nu_{FSR}} + N \psi_{rt} \right)}}{1 - r_1 r_2 e^{-i\left(\frac{\omega}{\Delta \nu_{FSR}} + N \psi_{rt} \right)}} \tag{3.1.20}$$

with mode number $N = 2p + |l|$, ψ_{rt} the Gouy phase accumulated after a round-trip inside the cavity and $\Delta \nu_{FSR}$ the cavity FSR frequency [12]. The other terms are the mirrors' amplitude reflectivities and transmittivities.

From eq.(3.1.16), it is clear that each term of the photocurrent is always the product of a CRF and its complex conjugate, but evaluated at a different frequency. This is a consequence of the squared module of the electrtic field and after some manipulations, this product can be written as follows

for two generic frequencies θ and Ω and a laser frequency ω.

$$F_{pl}^*(\omega+\theta)F_{pl}(\omega+\Omega) = (r_1^2+t_1^2) + \frac{r_1^2 + (r_1^2+t_1^2)\left[r_2^2 t_1^2 e^{-i\frac{(\Omega-\theta)}{\Delta v_{FSR}}} - 1\right]}{1 + r_1^2 r_2^2 e^{-i\frac{\Omega-\theta}{\Delta v_{FSR}}} - r_1 r_2 \left[e^{-i\left(\frac{\omega+\Omega}{\Delta v_{FSR}}+N\psi_{rt}\right)} + e^{i\left(\frac{\omega+\theta}{\Delta v_{FSR}}+N\psi_{rt}\right)}\right]}$$

$$\equiv A + \frac{B^+}{D_N^+}$$

$$(3.1.21)$$

where A, B^+ and D_N^+ notation are used to compress the formulation in the next equations. The +
or minis sign represents the frequency signal $\pm\Omega$ or $\pm\theta$. With this new formulation, all equations
similar to eq. (3.1.16) now become function of terms B and D, for both LG_{00} and LG_{10} modes and
considering Ω the modulation frequency, then:

$$\begin{pmatrix} \frac{\text{Re}_{pl}\left(I_{PD}^{\Omega}(\theta,\Omega)\right)}{I_0\,\text{Re}\left(c_{pl}d_{pl}^*\right)} \\ \\ \frac{\text{Im}_{pl}\left(I_{PD}^{\Omega}(\theta,\Omega)\right)}{I_0\,\text{Im}\left(c_{pl}d_{pl}^*\right)} \end{pmatrix} = \begin{pmatrix} 4A\cos(\Omega t) + \frac{(B^+D_N^{+*}e^{i\Omega t}+c.c.)|D_N^-|^2 + (B^-D_N^{-*}e^{-i\Omega t}+c.c.)|D_N^+|^2}{|D_N^+D_N^-|^2} \\ \\ i\,\frac{(B^+D_N^{+*}e^{i\Omega t}-c.c.)|D_N^-|^2 + (B^-D_N^{-*}e^{-i\Omega t}-c.c.)|D_N^+|^2}{|D_N^+D_N^-|^2} \end{pmatrix}$$

$$(3.1.22)$$

Of all these terms, only two needed to be calculated explicitly, for example $|D_N^+|^2$ and $B^+D_N^{+*}$, the
others are simply their complex conjugate or the same term calculated for the opposite sideband
frequency. The sum or difference of this $B^+D_N^{+*}e^{i\Omega t}$ term and its complex conjugate suggests that
the final result can be expressed as a function of cosine and sine, thanks to the Eulero identity. The
results are reported in the equations below.

$$|D_N^+|^2 = \left(1+r_1^2 r_2^2\right)^2 + 2r_1 r_2 \left[r_1 r_2 \cos\left(\frac{\theta-\Omega}{\Delta v}\right) + r_1 r_2 \cos\left(\frac{2\omega+\theta+\Omega}{\Delta v}+2N\psi\right)\right.$$
$$\left. - (1+r_1^2 r_2^2)\left(\cos\left(\frac{\omega+\Omega}{\Delta v}+N\psi\right) + \cos\left(\frac{\omega+\theta}{\Delta v}+N\psi\right)\right)\right]$$

$$(3.1.23)$$

$$B^+D_N^{+*}e^{i\Omega t} + B^{+*}D_N^+ e^{-i\Omega t} =$$
$$= 2t_1^2\left[\left[r_1^2 r_2^4(r_1^2+t_1^2)-1\right]\cos(\Omega t) - r_1^2 r_2^2 \cos\left(\Omega t + \frac{\Omega-\theta}{\Delta v}\right) + (r_1^2+t_1^2)r_2^2 \cos\left(\Omega t - \frac{\Omega-\theta}{\Delta v}\right)+\right.$$
$$+ r_1 r_2\left[\cos\left(\Omega t + \frac{\omega+\Omega}{\Delta v}+N\psi\right) + \cos\left(\Omega t - \frac{\omega+\theta}{\Delta v}-N\psi\right)\right] +$$
$$\left. - r_1 r_2^3(r_1^2+t_1^2)\left[\cos\left(\Omega t + \frac{\omega+\theta}{\Delta v}+N\psi\right) + \cos\left(\Omega t - \frac{\omega+\Omega}{\Delta v}-N\psi\right)\right]\right]$$

$$(3.1.24)$$

Considered a more general situation where $\Delta\psi \neq 2\pi$, then the equation shows that this phase shift needs to be added in the sine or cosine arguments in eq. (3.1.23) and (3.1.24) and subtracted in all the other terms with negative sideband frequency $-\Omega$.

These expression are useful because they are in sum for the I and Q error signal calculation, but they are subtracted in the case of the calculation of the PDH error signal starting from eq. 3.1.23. Another difference is that for the PDH error signal, the real part of eq. 3.1.23 do not present the first $4A\cos(\Omega t)$ but in exchange, a factor $4Ai\sin(\theta t)$.

A simulation was implemented with the cavity parameters, in order to study the consistence of these equations. In Figure 3.1 and 3.2 are reported the contributions of terms with positive and negative sideband for the imaginary and complex elements of eq. (3.1.22). It was considered an impedance matching Fabry-Perot cavity with mirrors' reflection coefficients $r_1 = r_2 = 0.994$ and no power leaks.
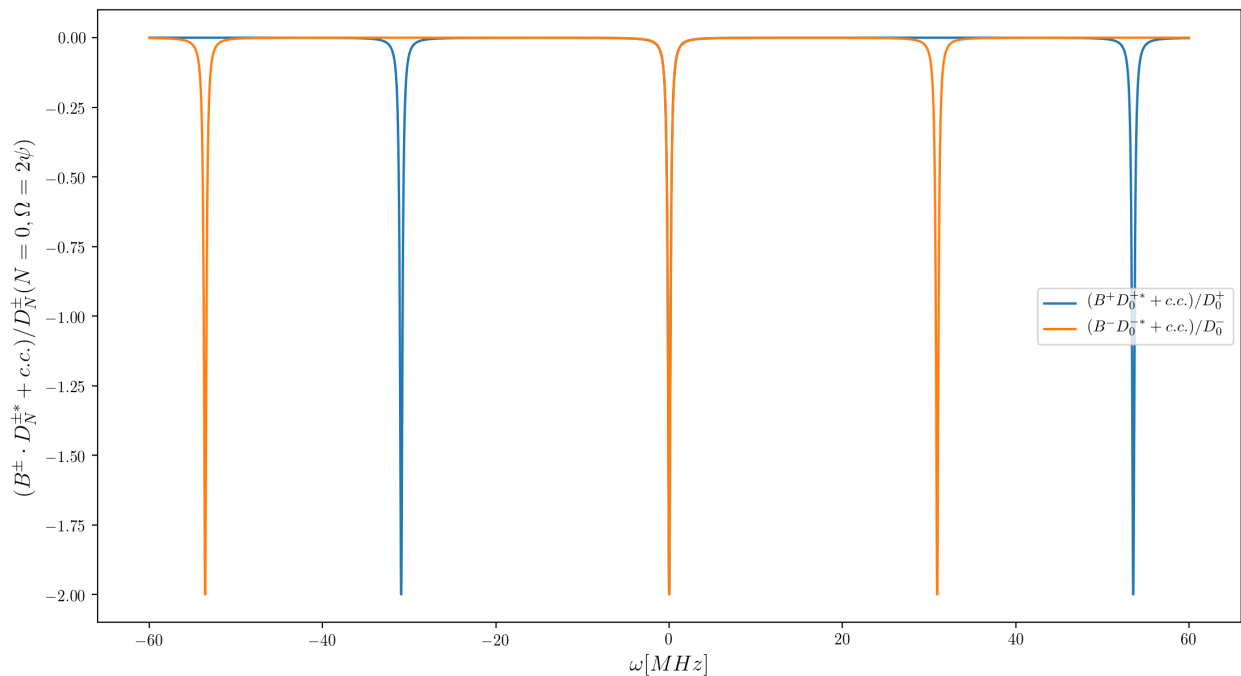
Figure 3.1: Contribution of the positive and negative sideband terms in the real part of eq. (3.1.22). The selected FSR frequency is $\Delta\nu_{FSR} = 84.5[MHz]$ and HOM distance of $\Psi_{rt} = 15.468[MHz]$.

In general, other two cavity situations can be described with these equations: the under-coupled situation ($t_1 < t_2$) in which the reflected field is more than the transmitted field and in this case the resonance peaks present higher amplitude than what was shown in Figure 3.1 and 3.2 and the over-coupled situation ($t_1 > t_2$), where the transmitted field is more than the reflected field (in this case, the peaks amplitude is lower).

In this conclusive step, the equations (3.1.22) are inserted in the reflected photocurrent of eq. (3.1.16) in order to retrieve the IQ signals. In the simulations it is possible to mathematically
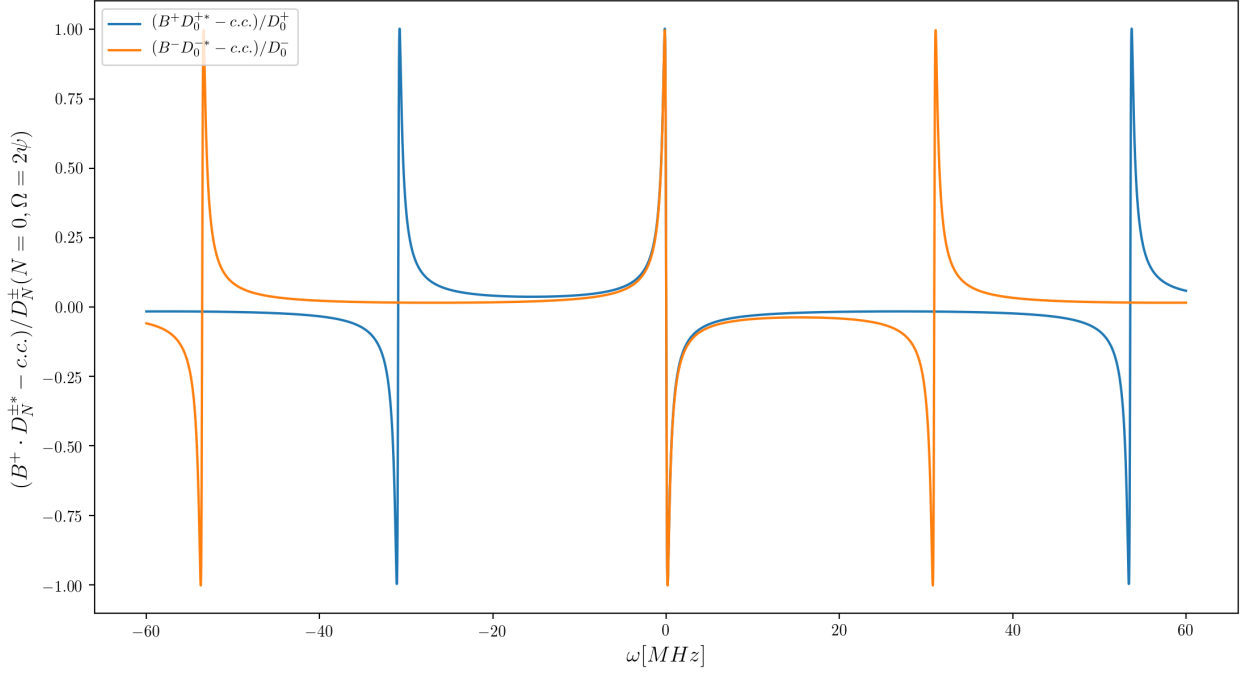
Figure 3.2: Contribution of the positive and negative sideband terms in the imaginary part of eq. (3.1.22). The selected FSR frequency is $\Delta\nu_{FSR} = 84.5[MHz]$ and HOM distance of $\Psi_{rt} = 15.468[MHz]$.

achieve the same effect of demodulation and low-pass filtering in a easy way. The I and Q signals present a phase difference of $\pi/2$ and I was considered in the simulations with a phase equal to zero. Then, thanks to the trigonometric identities, the I signal can be calculated with CRF term for $t = 0$ in both real and imaginary parts and and the real part has been multiplied for a minus sign. On the other hand, the CRF for Q is estimated with $t = \frac{\pi}{2\Omega}$ with no sign changes. This process was possible because only terms with the right modulation frequency were considered in the CRF.

I and Q signals calculation for ideal acquisition conditions

Attention now will be focused to I and Q error signals in ideal acquisition conditions. These conditions are achieved when the laser frequency is perfectly locked with the cavity (for this case, in the simulations this converts in $\omega = 0$) and one of the EOL sidebands frequency matches the LG_{10} mode frequency in a way that $\Omega = 2\psi_{rt}$. From these conditions, equation (3.1.19) was obtained and for this case, the I and Q module becomes

$$M_{IQ} = \sqrt{(\gamma^2 + \beta^2)(m_G^2 + m_B^2)} \tag{3.1.25}$$

and for this reason, the total beam mismatch with the cavity is defined as

$$Mismatch = \sqrt{\gamma^2 + \beta^2} \tag{3.1.26}$$

This ideal situation is used to test the correct implementation of the generalised equations into the simulations algorithm. With the same cavity parameters used before, the module M_{IQ} is calculated separately for a mismatch signal in β or γ up to 10%. Figure 3.3 shows that it is expected the same linear dependence for both mismatch types. In order to test a situation with a mixed nature mismatch, a phase term was introduced: the module ignores this oscillation term and the phase changes accordingly to it as required.
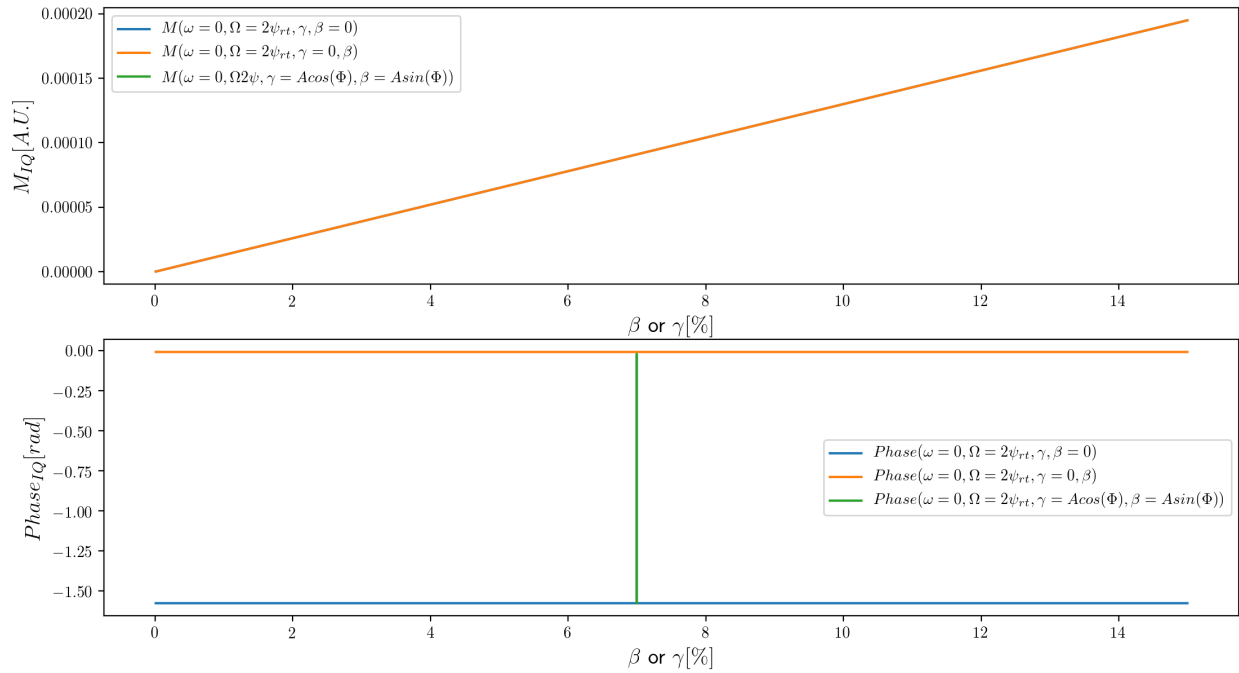
Figure 3.3: Linear dependence of M_{IQ} and phase with respect to different mismatch signals.

4 Simulations and effects of imperfections

Different system non-idealities were studied in order to delineate their effects in I and Q signals. A list is proposed here.

- The first important imperfection is the incorrect laser lock frequency.

- The second is a non optimal tuning of the EOL modulation frequency to the LG_{10} mode.

- A third one takes into consideration the second order terms in eq. (3.1.17).

- A fourth consists in a EOL Residual Phase Modulation or an EOM Residual Amplitude modulation.

- A fifth includes both EOL and EOM modulation effects in a more accurate approximation of the input beam.

Some of the described situations will be reported with a more detailed explanation in the next sections. Before that, it is helpful to divide the list elements based on their nature as mathematical approximation effects or physical effects. This was done because the experimental data include acquisitions with mismatch up to 10% and the first order approximation loses its validity for those big mismatch values.

4.1 Second order approximation

The introduction of the second order terms in eq. (3.1.17) causes an asymmetry in the module dependence from the two sources of mismatch. The effect is appreciable in Figure 4.1. In this plot, all generic situations with mixed mismatch sources are positioned in between the two module curves that represent a pure waist or pure position mismatch.

4.2 Laser lock frequency

If the PDH method for the cavity lock is not perfect, then it is expected that the laser frequency ω is different from the cavity resonance frequency. Studying how the error signals change with
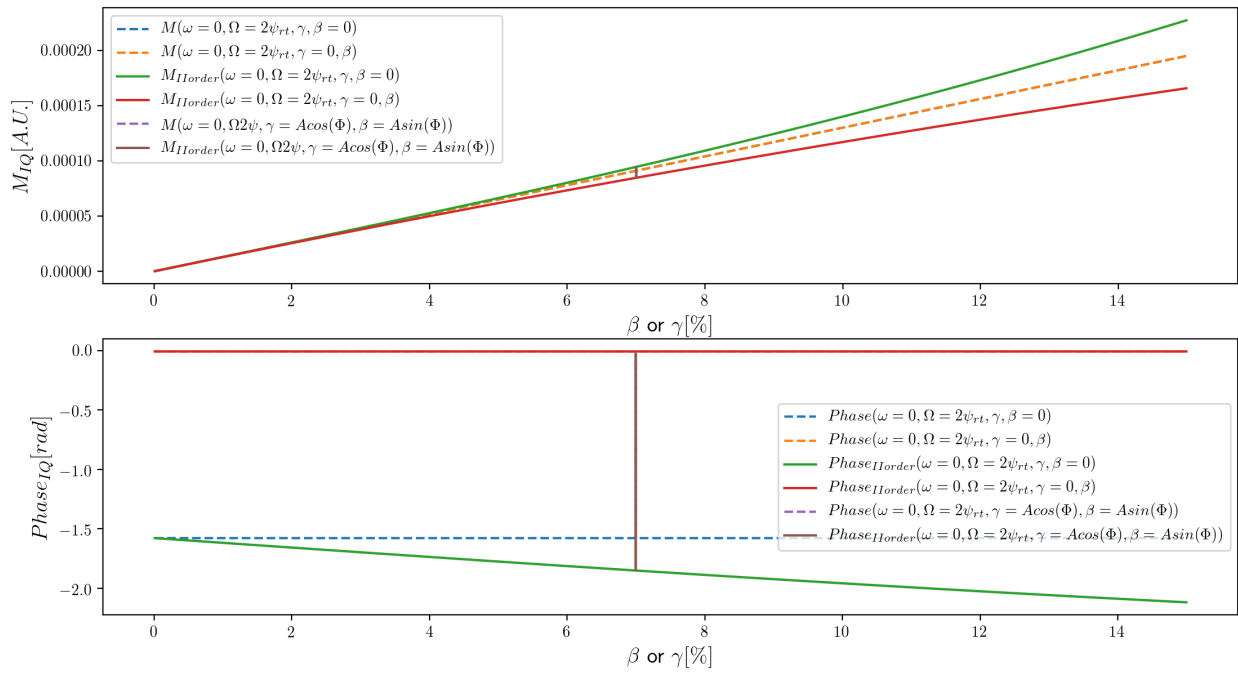
Figure 4.1: Confrontation of the first and second order approximations of the coefficients (3.1.17). The effect is a slight deviation from the linearity and the module value now behaves differently for the two type of mode match signals.

this imperfection is important because its contribution is present in the first order approximation and the noise produced can cover the wanted I and Q trend. In Figure 4.2 it is possible to scan the simulated I and Q error signals changes. To experimentally reproduce this trend, a cavity scansion could be used. This Figure can give a proof of the necessity to work with an optimized laser feedback loop. For this reason the estimation of the working range in between the bimodal signal needed to be checked before the complete application of this mode mismatch sensing method. To show the differences of the first and the second order approximations, a high value of mismatch was selected, but the effect of this imperfection still remains the biggest source of error.

4.3 EOL modulation frequency

Another possible source of error for this technique is the imperfect match between LG_{10} high order mode spacing and the sideband frequency. This generates a lower error with respect to the laser lock imperfection as it can be seen in Figure 4.3. Also in this case, the second order approximation minimally change the module, but its effect is more appreciable in the phase shift. This shift corrects the module minimum near zero, where it is expected to find the resonance between the sideband and the cavity mode.[1] These simulations give an estimation of the modulation frequency range in which it is advisable to work with.

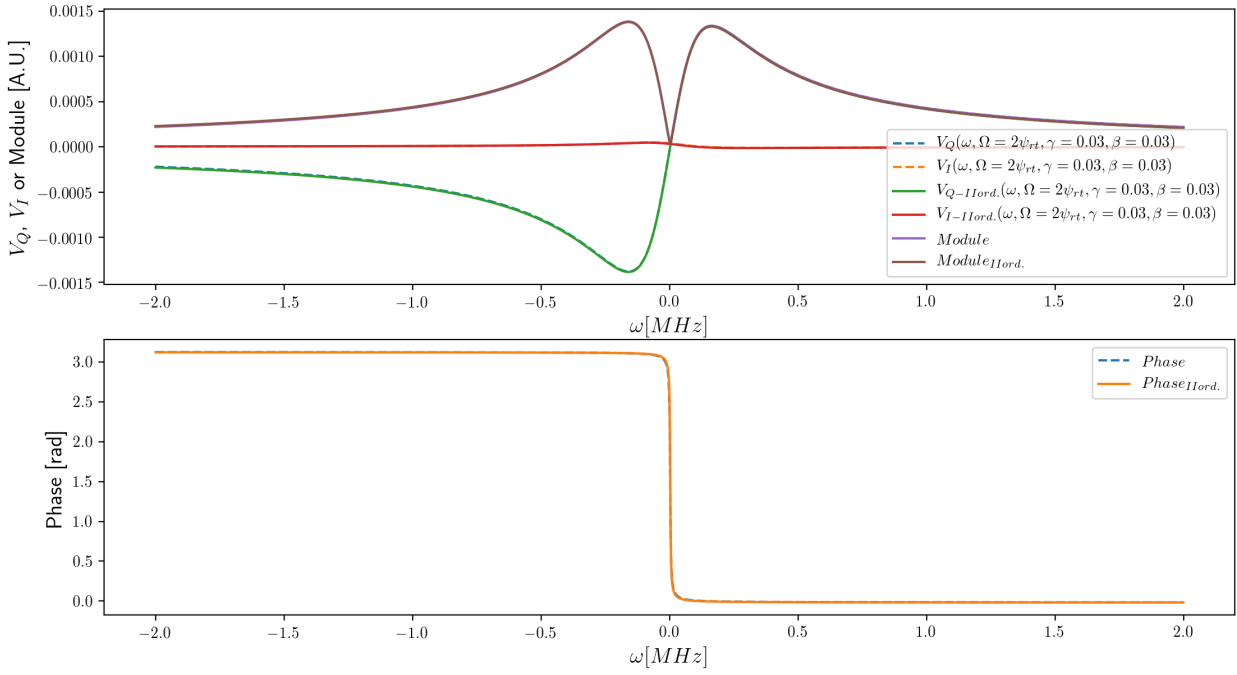[1] As a side effect, this method could be used to give a finest estimation of the cavity HOMS spacing.

Figure 4.2: Simulations of the voltage signals as a function of the carrier frequency offset from the cavity resonant frequency.The cavity LG_{00} resonant frequency correspond to zero.
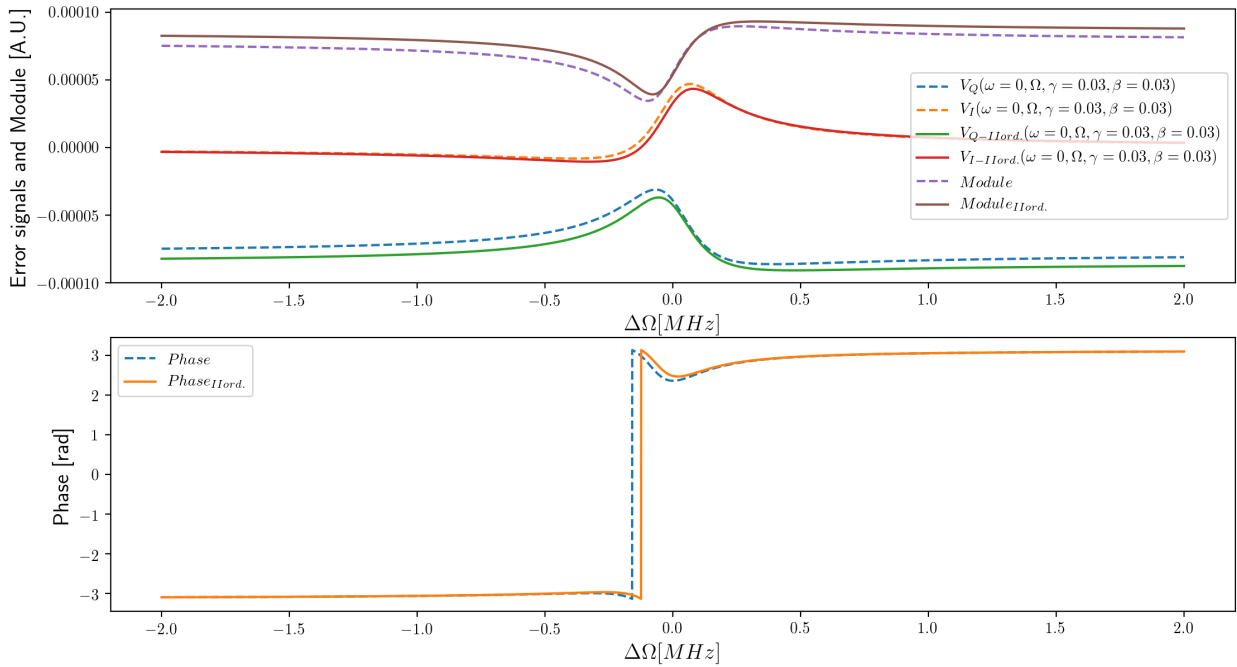

Figure 4.3: Simulations of the voltage signals in presence of a not coupled sideband frequency with the cavity mode LG_{10}. In the x axis it is reported the difference of these frequency $\Delta\Omega = \Omega - 2\psi_{rt}$

4.4 EOM and sidebands couplings

As it was already anticipated, for this mismatch sensing technique, two different modulation process are required. The first is generated by an EOL device for the PDH technique and the second by a dedicated EOL device to retrieve the wanted I and Q error signals proportional to mismatch. The EOM device generates phase modulations for all the laser components and the effect is described in eq. 2.4.9. For the analysis proposed in this section, only terms up to the first order were considered. This was done to introduce second order correction in the I and Q signals as it happens after the module calculation. The reason of the introduction only of the second order was because higher order terms, introduce effects at least of the third order in the retrieved photocurrent (the signal intensity is proportional to the squared module of the electric field). The calculation shows that the EOL and EOL sidebands coupled to each other after the demodulation process. The dependencies from the EOM modulation index in the equation appears in the EOL and EOM coupling terms with a power of two. In Figure 4.4 the simulation was calculate for values of $\varepsilon = 0.04$ and 0.4. The set EOM modulation index after the characterization described in chapter 7.1.4 is similar to the value used for these simulations. These simulations were used as a starting model to interpret the experimental signals behaviour studied in this thesis.
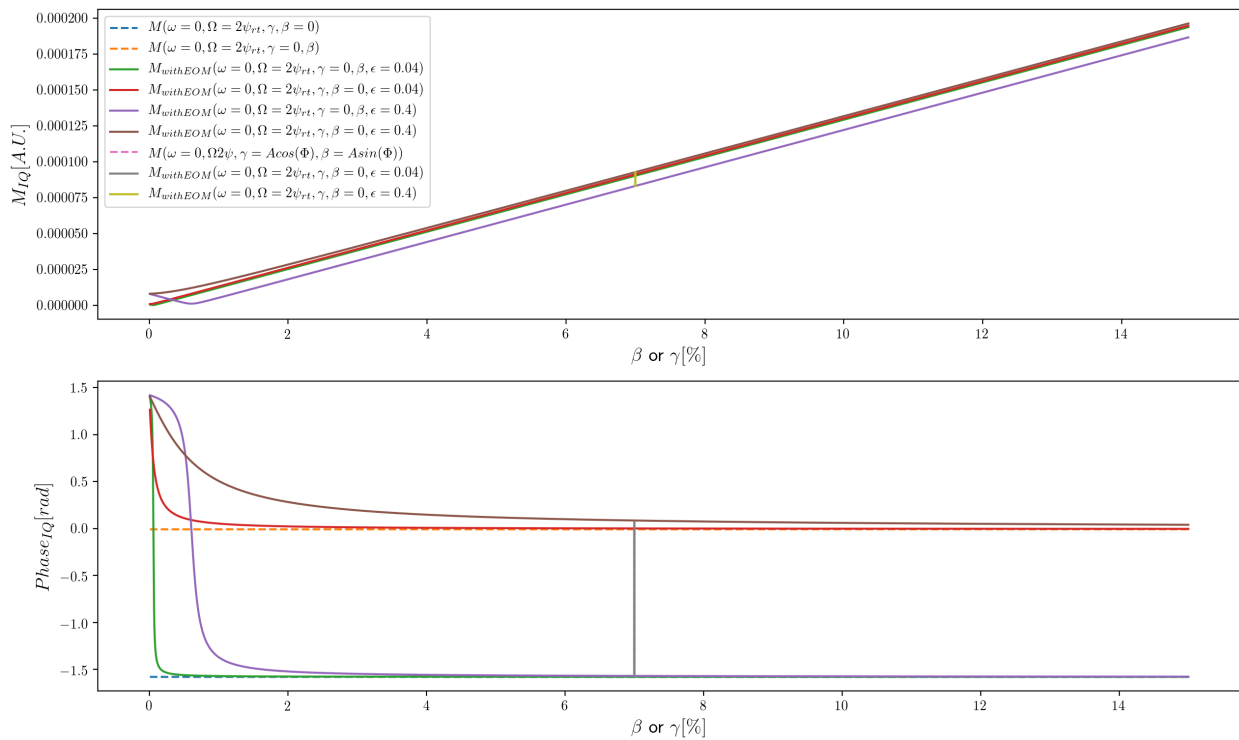

Figure 4.4: Simulations of the EOM effect for different values of the index modulation ε.

5 Experimental setup

To implement the studied RF mode sensing technique an experimental setup had been built prior to the start of this thesis work in Laboratori Nazionali di Legnaro (INFN-LNL). The experimental setup is composed of two parts: the first contains all the optical components mounted in an optical table; the second part includes all the electronic components required for data acquisitions and for controlling the optical elements. The design and a more detailed explanation of the construction parameters can be found here [6].

In the next sections the main components are presented with more details, starting with the optical elements, with a specific care of the description of the EOL device and in conclusion a description of the electronic elements.

5.1 Optical table

In this section the optical elements in the optical table are described. For a better understanding of the setting, take as a reference the marked elements in Figure 5.1. In the Figure, the initial laser beam path (in red) is shared with other two different experiments and and some of the elements on this red optic line til the BS_FIBER are not part of this experiment. The laser source is a Nd:Yag crystal that emits light at 1064 nm and it has an integrated piezo used for the feedback loop of the PDH technique.

(a) The EOM is the first important device that the laser beam interacts with, in the dedicated optical line. It is a commercial resonant EOM operating at RF frequency of 13.45 [MHz] and the voltage applied to its crystal is generated by a DDS RF generator described in the next section.

(b) The EOL crystal is clamped in a dedicated support and powered by another RF signal which frequency was set after the detailed study reported in the next chapter.

(c) The two lenses L13 and L14 were implemented as a telescope in order to produce desired mismatch signals to test the response of the I and Q signals.

(d) The triangular cavity was designed with two flat mirrors and a curved mirror. The cavity is a impedance matched cavity with $\Delta \nu_{FSR} = 84.5$ MHz and a cavity linewidth of 686.8

kHz and a finesse of $\mathcal{F} = 386.5$. The beam light is transmitted from the first flat mirror and enter inside the cavity, the reflected light from this mirror is acquired and used for the generation of the error signals. The transmitted light interact with the second flat mirror and the transmitted light is acquired.

(e) The light transmitted from the second flat mirror is acquired from a single-element photodetector and used to study the cavity properties and control the correct laser lock procedure with the PDH technique.

(f) The last single-element photodetector is dedicated to acquire the cavity reflection beam. Its electronic is designed to split the generated photocurrent and use one component to generate the PDH error signal, a second is sent to the electrionics for an external elaboration and retrieves the I and Q error signals, the others two components are used to control.
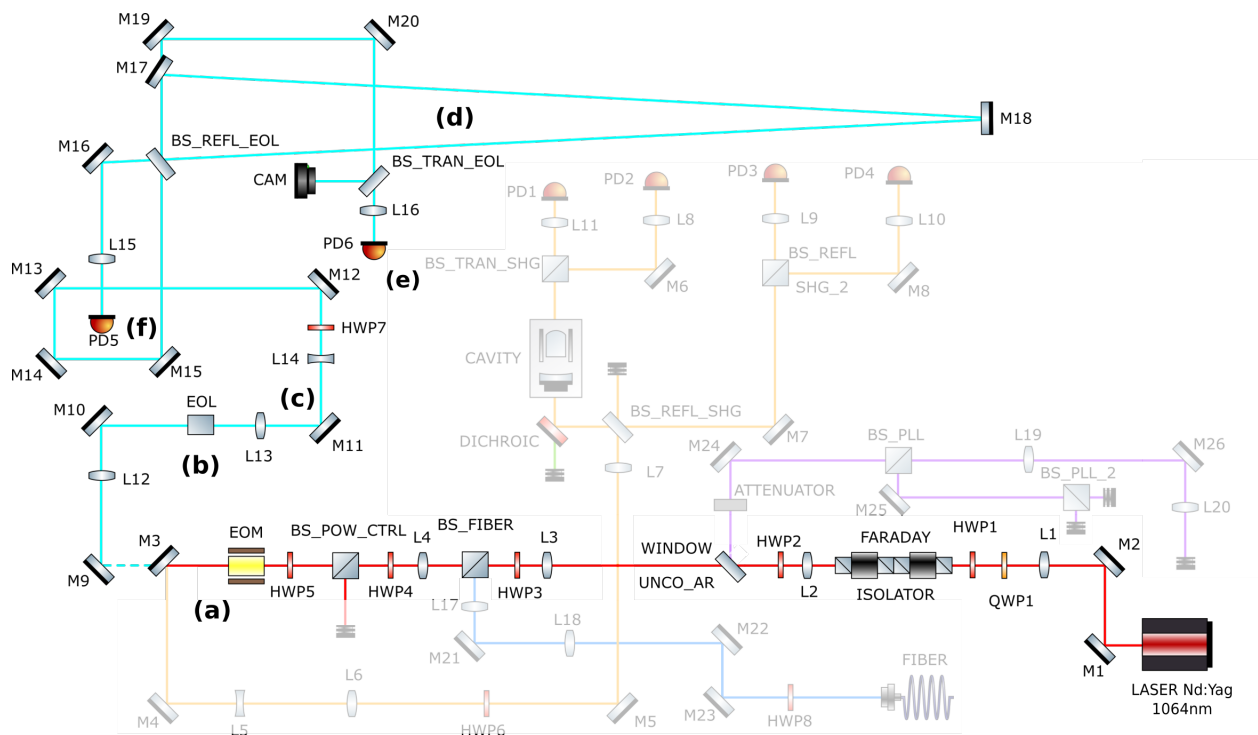
Figure 5.1: Scheme of the optical table, the light blue line represents the optical path from the elements of the dedicated setup for this sensing technique. The initial laser beam path (in red) is shared with other two different experiments.

5.2 EOL device

The present EOL device was designed as a sandwich of two set of electrodes that enclose a Lithium Niobate crystal in between. The electrodes were designed to generate a lens effect inside the crystal and the project details can be found here [6]. The crystal length in the direction of the optical axis was set in order to respect the optical line limitations after the EOL device and to maximize the number of electrodes and consequently the number of lenses generated inside the crystal. With

these considerations, four biconcave electrodes were applied at top and bottom of the crystal. In Figure 5.2 shows a finite element simulation of the electric field performed to optimize the design of the electrodes. The idea behind this project is the realization of a device that can induce RF modulation of the beam mode LG_{10}. This device was designed to behave as a lens that can change its refraction index, based on the voltage applied to its electrodes.
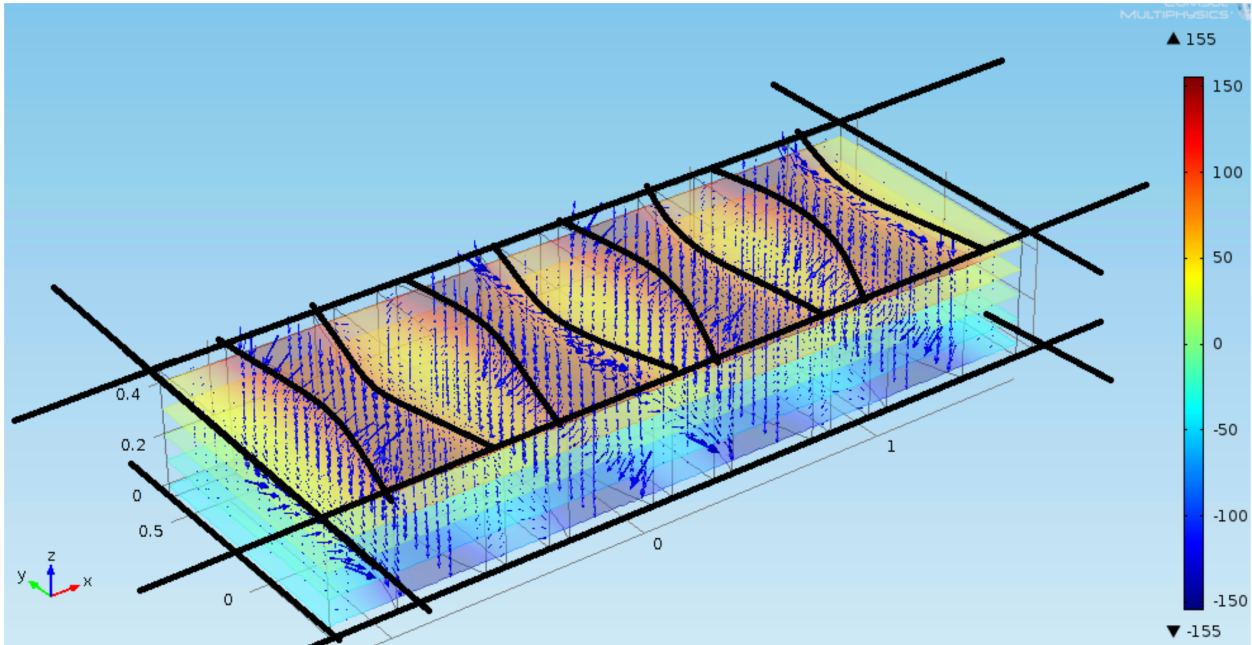

Figure 5.2: Graphic representation and simulation of the electric field distribution inside the Lithium Niobate crystal. the black sketch represents the boundaries of the electrodes [6].

5.3 Electronic scheme

This section is dedicated to the electronic scheme, summarized in Figure 5.4, in which elements with a similar or related function are grouped by colors.

1. **Amplifier and Power supply group (Light blue):** two different electronic chains are included, the power supply chain for the photodetectors and the one required for the laser feedback loop, including the amplification stage.

2. **RF signal generation group (white):** The DDS RF generator is used to generate all four independent modulation/demodulation RF signals that are phase matched one to each other.

3. **Electronic to Optics group (violet):** in this group it was considered all the optical elements that require electronic signals to perform their function or to be controlled. They are three:

    a) **EOM:** the RF signal generated by the DDS RF generator is directly connected to the EOM's electronics and then applied to its crystal.
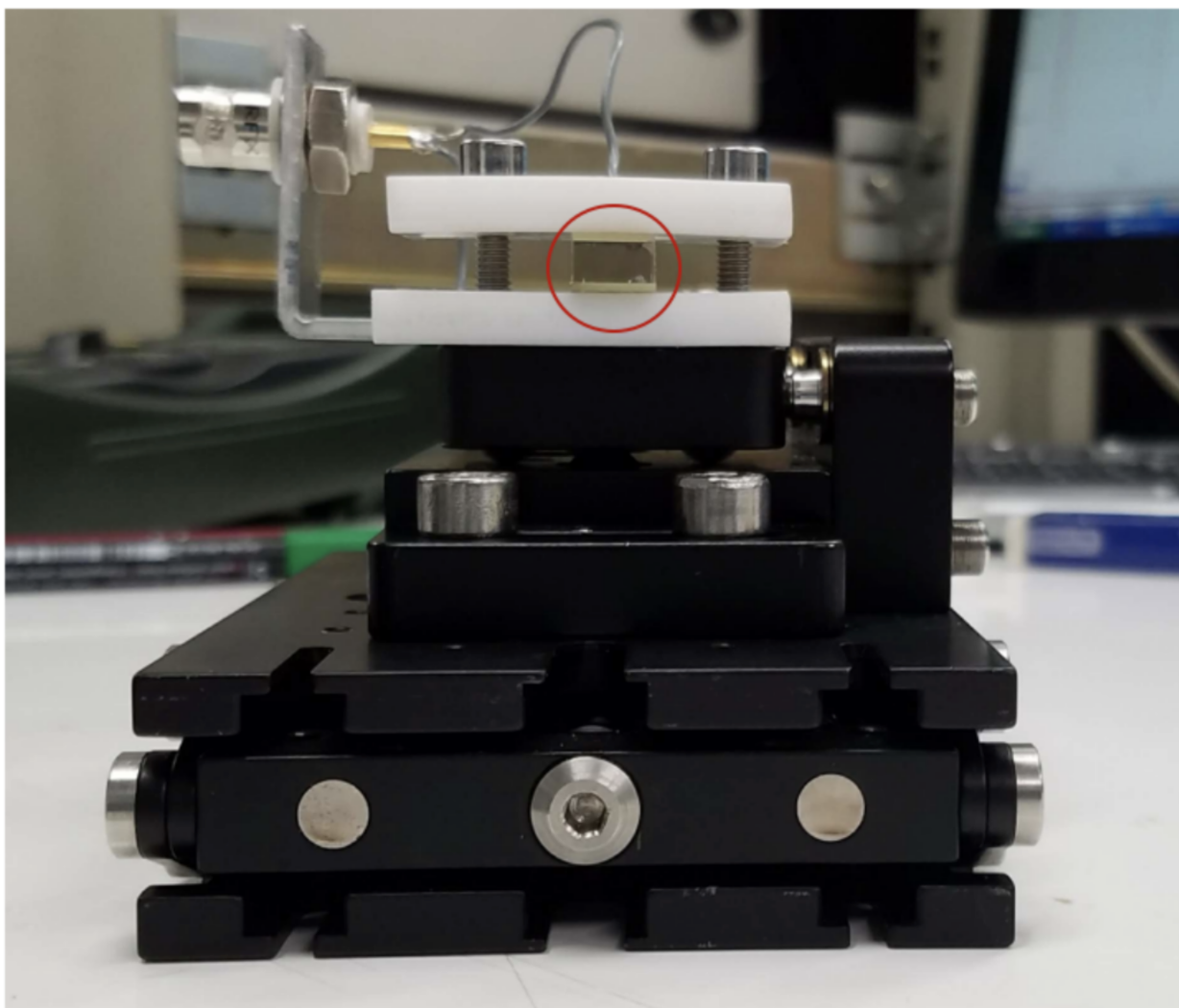
Figure 5.3: A photo of the described EOL device. The red circle highlights the crystal entrance face. The edges of the top and bottom PCBs that support the conductive paths serving as electrodes are visible above and below the crystal. [19].

b) **Laser:** the actuation signals from the power amplifier output are sent to the laser piezo, , afecting the frequency of the emitted light; this step is used for the feedback loop to lock the laser frequency or thanks to a ramp signal to perform a frequency scan of the cavity

c) **EOL:** the DDS RF generator signal is connected to a dedicated power amplifier and sent to the electrodes.

4. **Photodiodes group (yellow):** the single-elements photodiodes produce current signals proportional to the incident light intensity integrated over all their detector surfaces. Both photodiodes possess a dedicated electronic board that modifies the acquired current in a way that it is possible to retrieve: DC component, RF component and demodulated component. For the last signal, an RF signal is required as an input.

5. **Demodulation group (green):** the I and Q signals are elaborated with the same acquisition steps. The only difference is that the local oscillator signals used for demodulation have a phase difference of $\pi/2$. They were obtained thanks to a power splitter (ZMSCQ-2-50+) from the same DDS RF signal. In input, the RF signal from the photodetector in reflection is divided by a power splitter and mixed with the local oscillator signal. The mixer output is then low-pass filtered at 0.03 Hz and 6 dB/Dc and acquired using the PXI platform.

6. **Acquisition/actuation group (pink):** this stage considers two elements:

a) **PXI:** a digital system based on the National Instrument PXI platform is used to acquire a variety of signals using and ADC and a connector box (only the latter is shown in figure 6.4). The acquisition system is connected to its dedicated hardware with a personal computer. This setup is used to acquire the I and Q signals.

b) **MOKU:lab:** this instrument uses a FPGA to acquire, analyse, and generate signals. Its output is connected to the electronic chain dedicated to the laser piezo actuation and it is used to control the laser frequency, for both cavity scan and PDH feedback loop. It was used tor the cavity scan and the PID control error signal acquisitions.
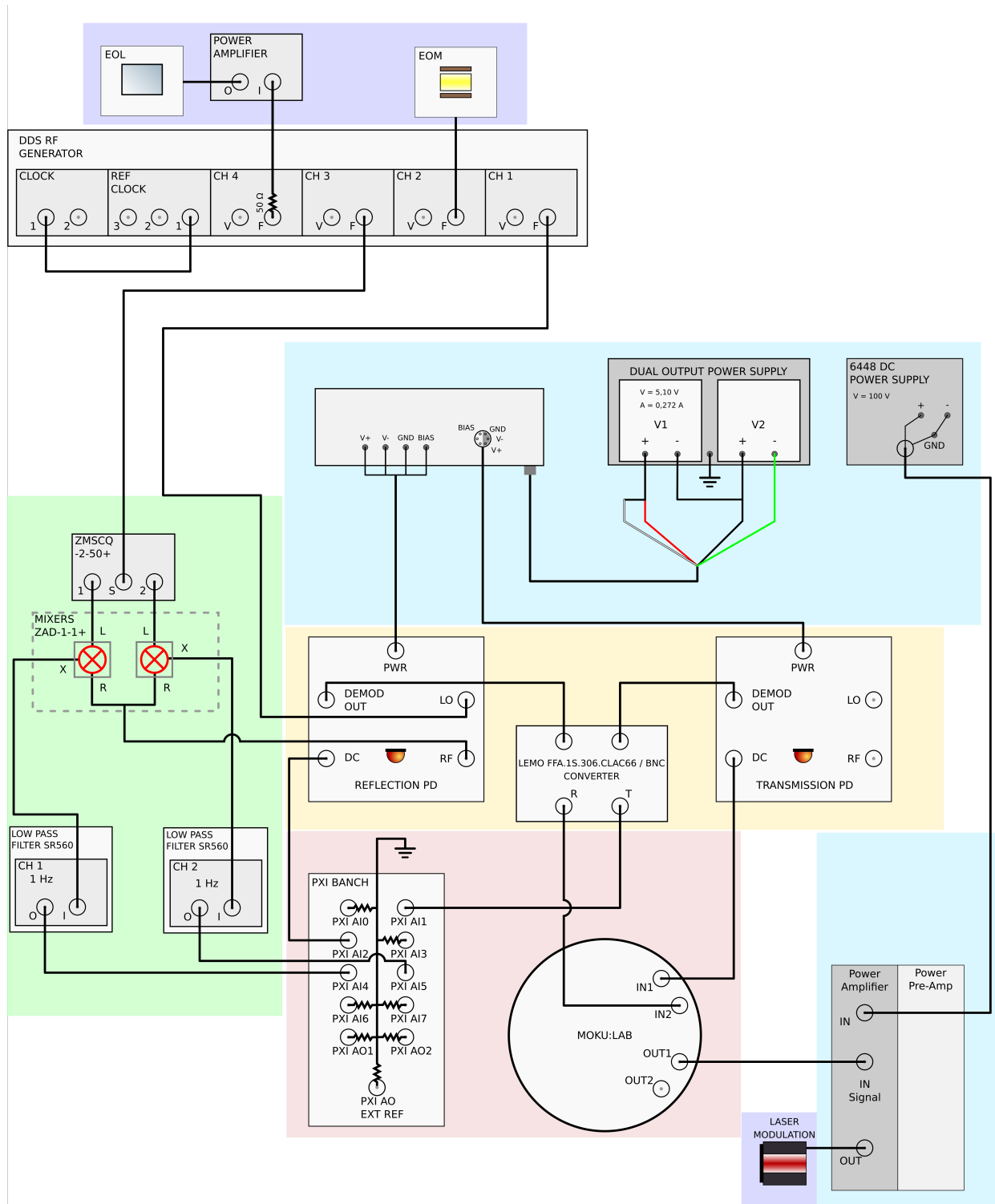
Figure 5.4: Scheme of the electronics used in this experiment. In blue the power supplies step. In violet the connections between the optical crystals (laser included) and the electronic elements. In green the electronics for demodulation and L-P filtering. In yellow the Photodiodes in transmission and reflection. In pink the acquisition instrument: Moku:lab and PXI. In white the DDS RF generator.

6 Measurements

This chapter is dedicated to present the experimental activity done in the laboratory. Measurements were taken between November 2019 till the beginning of March 2020 and restarted in June due to Covid-19 pandemic. The first part of the laboratory activity focused on the characterization of the cavity and laser lock parameters for the PDH technique. The EOL modulation was turned off for these studies aimed at finding a suitable working condition with a stable feedback loop response. At this point it was possible to confidently proceed with the effect characterization of the EOL device effects. At the end the desired I and Q error signals measurements was acquired and analysed.

6.1 PDH optimization

In more detail, the PDH sample rate and data loss problems optimization focused on the study of the Moku:lab PID controller parameters and the lock stability for different EOM index modulation values. The optimization of the feedback loop parameters were necessary of the recent introduction of the Moku:Lab in the feedback loop. Before, the loop control was done with the PXI module and a dedicated developed LABView program, but the lower acquisition frequency limited the performance of the feedback loop.

The PDH method, as it was described in the theoretical introduction, uses the error signal generated from the photocurrent in reflection, after demodulation at the EOM frequency.

In an ideal situation, this error signal is zero when the laser frequency match exactly with the cavity LG_{00} mode frequency. Near this condition, the error signal changes with a linear dependence from the difference between the laser and LG_{00} frequencies.

In conclusion, the desired laser lock feedback loop need to respect three conditions:

- the lock condition needed to be maintained stable for long periods of time (at least of 10 minutes for this experiment)

- with closed loop it is possible to obtain a transmitted signal as constant as possible for long time intervals (at least 10 minutes),

- the error signal mean value needed to be as close as possible to the reference value in a way that the transmitted power is at its maximum.

- the error signal fluctuations needed to be as little as possible. A first quantification can be

given with the error signal RMS and in absolute terms, a little fraction of the cavity linewidth.

A PID controller is a proportional–integral–derivative controller. Its algorithm generates continuously an actuation signal by summing three values proportional to the value, the integral and the derivative of the difference between a desired fixed value and an error signal. Thus, three numerical values needed to be estimated and set to characterize the proportional, integrative and derivative elements of this algorithm to reach a stable look condition. The algorithm with these three parameters actuates as a frequency filter. To set optimal filter parameters in our experimenst, the error signal distribution has been studied.

6.1.1 PID filter description

This section describes the Moku:lab PID controller interface and presents the features used in the acquisition process. An example of its interface when used as a PID controller is shown in Figure 6.1. Reading the interface from the left, the controller receives Moku:lab's input channels (In1 and In2) and composes them with the matrix coefficients (in this case, we simply map input 2 on the controller channel that uses output 1, and ignore the other input). The matrix outputs are elaborated by two dedicated lines and then the output signals are sent to the Moku:lab output ports. Each line allows for the introduction of an Input Offset (IO) before the filter and an Output Offset (OO) after it. The filter can be costumized thanks to six built-in filter parameters that are:
P (Proportional gain), I+ (Double integrator crossover frequency), I (Integrator crossover frequency), IS (Integrator saturation level), D (Differentiator), DS (Differentiator saturation level).

The colored Probe A and Probe B in Figure 6.1 can be plotted in the dedicated area or saved to disk. With the measurement tools it is possible to analyse the probe signals in real time end extrapolate for example the mean value or the standard deviation. It is possible to find more detailed information about this interface here [20].

6.1.2 Study of error signal and offsets

The PID controller data acquisition functionality was used to save and analyse the PDH error, the transmitted DC and the actuation signals in order to optimize the filter paramters.
This section is dedicated to the study of the error signal distribution with different Input Offset (IO) and Output Offset (OO) configurations.
With an ideal filter, the two offset cover two different roles. The Input Offset is added before the controller filter, so it shifts the working point at which the filter tries to minimize the error signal; it can be used to compensate unwanted electronic offsets that may shift the zero of the error signal away from the intended physical working point. The expectation is that the center of the error signal distribution follows this offset value. The mixing matrix was set in a way that the error signal from In2 was injected in the upper line with a factor -1. In an ideal filter implementation, the
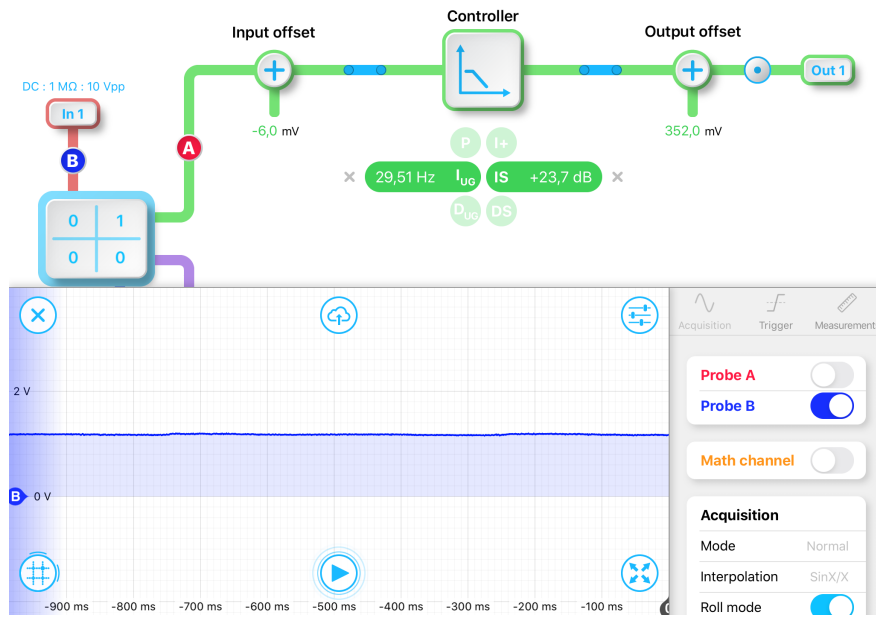
Figure 6.1: Moku:lab PID cotroller interface.

infinite gain of the integral part at zero frequency would completely cancel out the output offset; in a real implementation this may not happen both because of signal saturation and of limited gain at low frequency.

On the other hand, the Output Offset is added to the already calculated actuation signal, so it can be used to move the laser frequency close enough to the working point that the error signal is suitable to engage the automatic feedback loop. In this situation, the OO can be change freely because now it is viewed by the filter as an additive constant to the actuation signal (in a real setup, the OO can change only in the voltage interval that can be produced and sent to the laser).

In the experimental data, the error signal distribution was observed by studing its amplitude histogram. Figure 6.2 shows an acquisition of error signal and transmission signal. Both histograms to the right side describe the error signal distribution, in the upper case the x axis is in Volt and in the bottom case it was calibrated in MHz. [1] The last histogram can be used to estimate the error signal fluctuation around the cavity LG_{00} frequency and with a direct confrontation with the cavity linewidth, it is possible to estimate the effective fluctuation range around the peak position.

The first effect studied was the one generated by the Output Offset and the results are shown in Figure 6.3. Setting the I O value to 0 V, and then closing the feedback loop, the OO was changed with regular steps until the lock condition was lost. The transmitted amplitude changed in the during the acquisition process because of drifting room temperature and the FWHM plot shows that the lock condition worsened for the last acquisitions (the acquisition started from the lowest

---

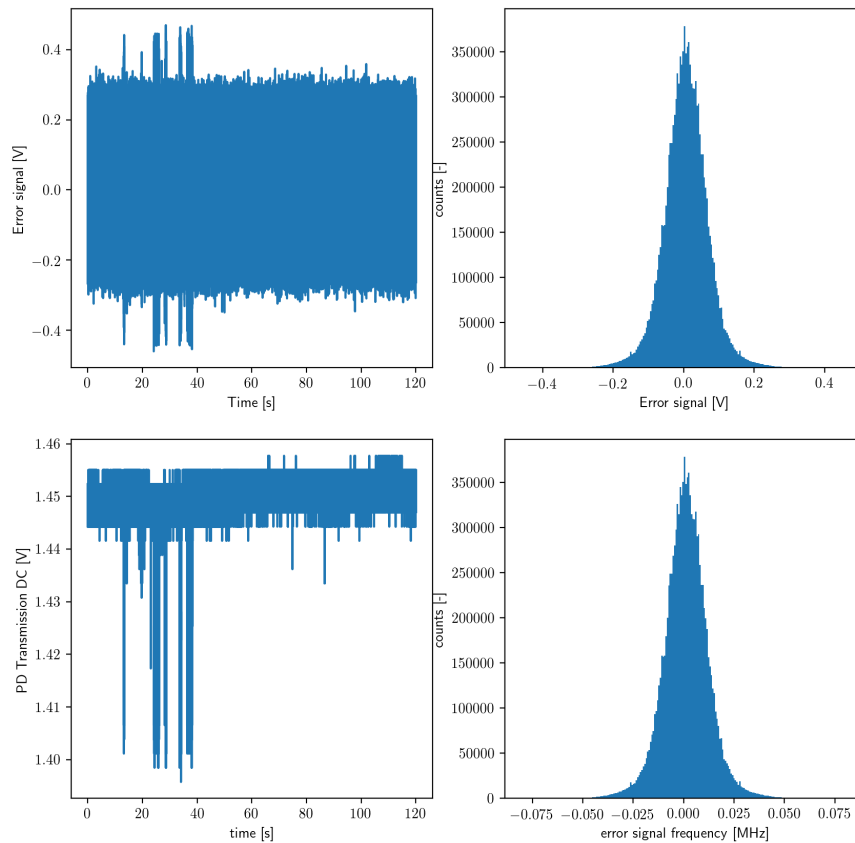[1]The method to generate the calibration curve is presented in the next sections.

Figure 6.2: Acquisition of the error signal and cavity transmitted DC signal from the Moku:lab PID controller interface. Left: record of both signals. Right: histograms of the error signal voltage distribution. Bottom: error signal distribution of the calibration in MHz of offset from the desired lock frequency. If this value is compared with the cavity linewidth, then it is possible to estimate the effective fluctuation range around the peak position.
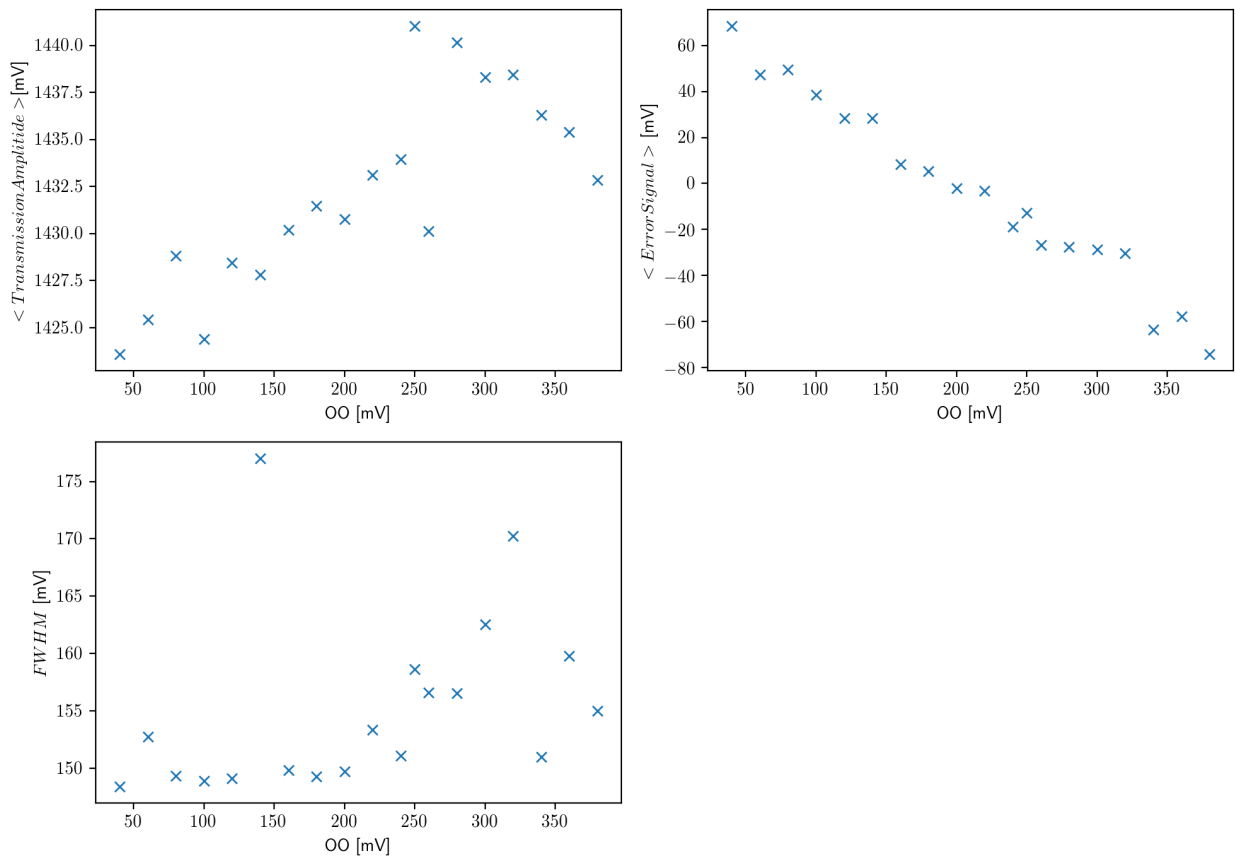
Figure 6.3: Analysis of the Output offset (OO) effects in a closed loop condition and with a constant Input Offset. Top-Left: mean value of the transmitted power as a function of OO, this plot shows a jump in the laser amplitude right in the middle of the acquisition process probably due to the uncrontrolled environment (our cavity is in air and the room temperature stabilization is underperforming). Top-Right: estimated mean value or center of the error signal as a function of the OO. Bottom: study of the error signal FWHM of the error signal distribution.

OO value). After the acquisition process, the cavity was found to be misaligned.

From these measurements it was possible to advance the hypothesis that the filter cannot completely compensate for lower frequency noise, as it can be the manual introduction of an offset. The general strategy is to manually actuate on the OO to maintain the lock at the correct frequency.

The same procedure was followed for the Input Offset and a linear trend from the error signal mean value with respect to the IO was found as it was expected for this case. Nevertheless, if the closed loop condition was maintained for long periods of time, it was observed with the Moku:lab PID controller live measurements tools that the error signal mean value shifted slowly with time. This behavior is explained by the fact that the laser do not compensate for temperature changes and to compensate the working point shift the OO can be used.

To study if in in the feedback loop are present resonances or autooscillations, the Power spectral Density (PSD) and the RMS were calculated. Thanks to them qualitative observation, it was decided to change the filter gain at lower frequencies in order to reduce the PSD components and resonance peaks at lower frequency.
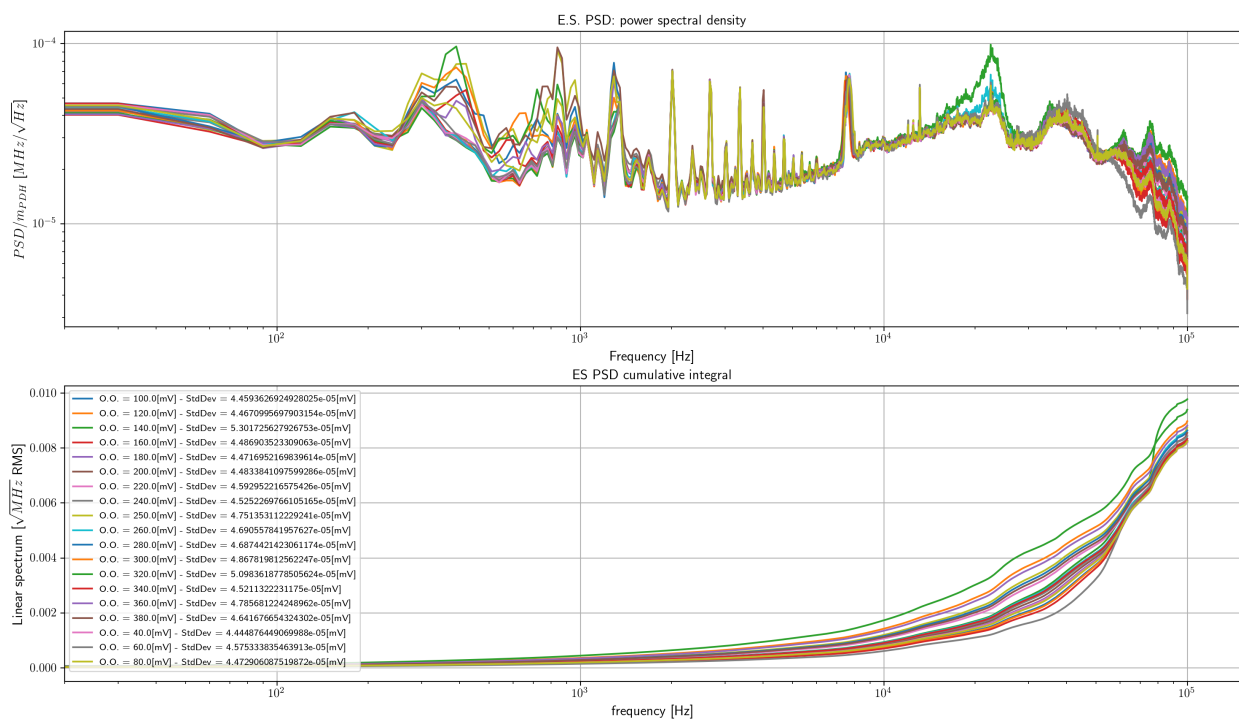

Figure 6.4: Studies of the Power Spectral Density and RMS for the presented measurements of the OO effect to the feedback loop. The presented PSD has mmany resonances peaks and the different acquisitions changes their behaves for the resonances at 400 Hz and 20 kHz.

6.1.3 PID filter parameters optimization

To conclude the optimization of the Moku:lab filter parameters, the effect of the Iegrator Saturation level (I.S.) on the control loop is presented. This parameter influences the total gain for lower

frequencies. This was necessary because of low frequencies drifts in the laser power delivered to the experiment (again due to an underperforming temperature stabilization of the room). This set of acquisitions was taken with the closed loop. This decision was taken to maintain the same lock condition and offset values and focus only on the I.S. effects. Figure 6.5 shows that increasing the low frequency gain, the residual offset from the working point is reduced, as expected and discussed in the previous section. However, above a certain value the offset does not improve anymore, the average transmitted intensity starts to drop and the FWHM of the error signal increases substantially.

The opposite happens for lower I.S. values, the transmitted signal and the error signal FWHM are optimized, but the error signal mean position did not follow anymore the reference value.
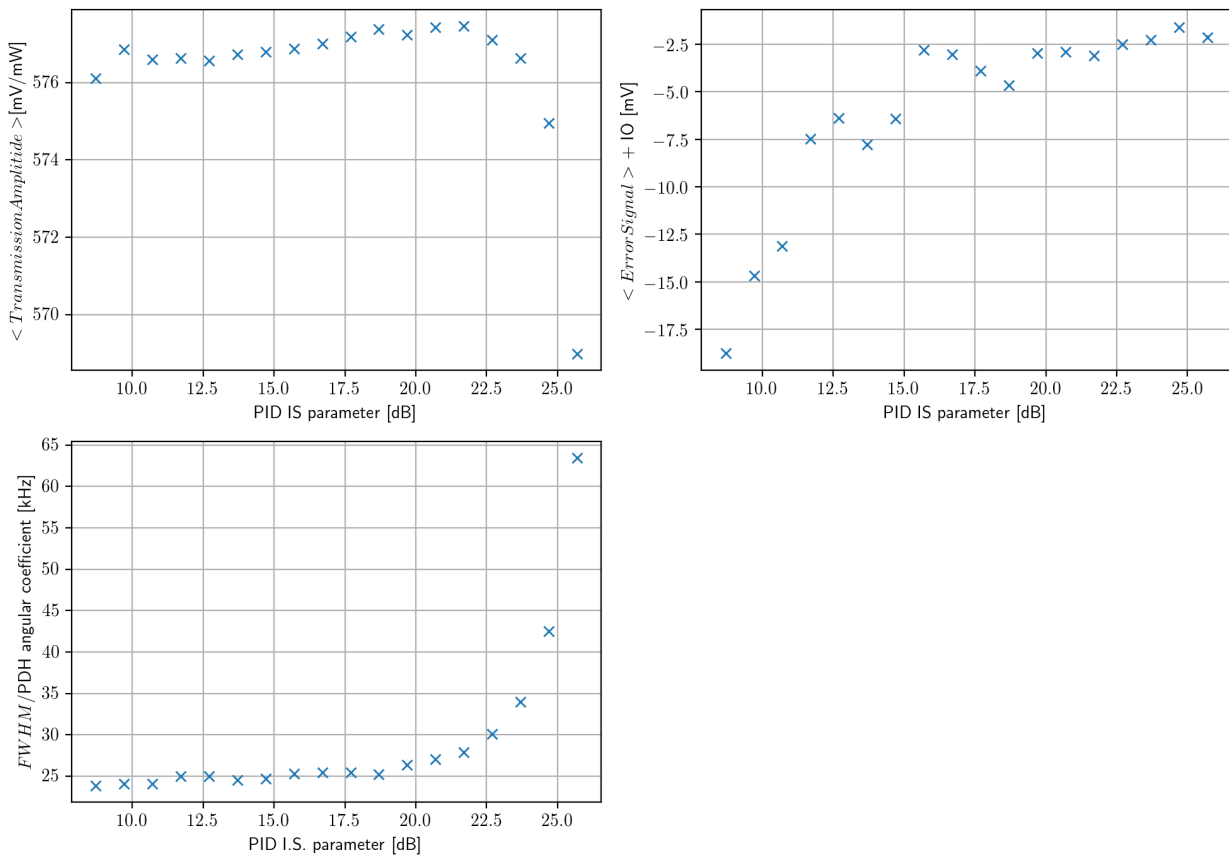

Figure 6.5: Error signal studied for different Moku:lab PID controller I.S. parameter (it controls the total gain at low frequencies). This plot shows the Power Spectral Density of the Error signal (PSD) and the RMS. Higher gain reduces low frequency fluctuations, but at the same time induces a resonance for higher frequencies and consequently a lock instability.

From Figure 6.6, it is possible to confirm the above description and estimate which frequencies components introduce instability. While low frequency components are generally reduced with increased IS, they don't improve noticeably above IS = 20; however, past this value a strong resonance around 20 kHz is triggered and spoils the overall performance of the loop.

Thanks to these observations, the I. S. was fixed ad 18 dB, to further increase stability at low
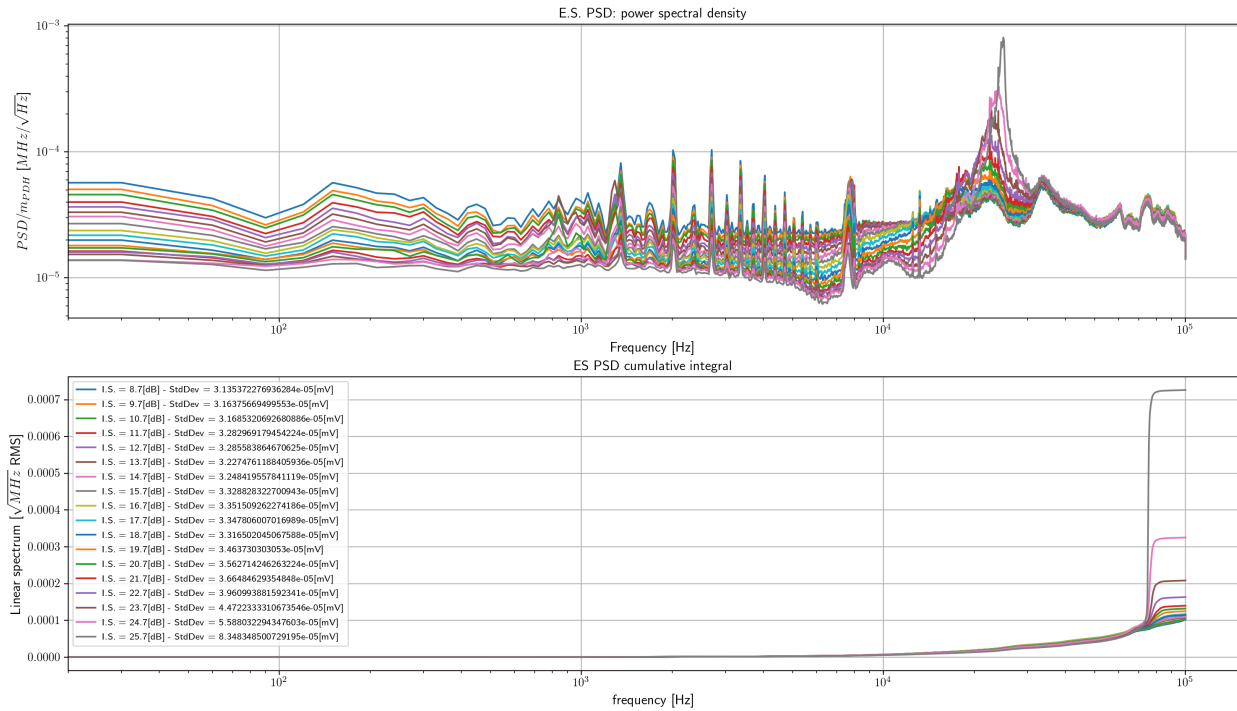
Figure 6.6: Scansion of the Moku:lab PID controller I.S. parameter (total gain at low frequencies). This plot shows the Power Spectral Density of the Error signal (PSD) and the RMS. Higher gain reduces low frequency fluctuations, but at the same time induces a resonance for higher frequencies and consequently a lock instability.

frequency without triggering the 20 kHz oscillation, a double integrator stage was introduced (as discussed in Figure 7.1.2)

6.1.4 Final performance and optimization of EOM modulation index

With a preliminary stable lock, now it is possible to proceed with the optimization of the EOM modulation index to further increase the lock stability. Normally, the PDH error signal slope around the cavity resonance frequency, and thus the overall gain of the loop, can be approximated linear dependency from the induced modulation index. A change in the slope of the error signal influences directly the loop performances [21]. From the simulations clearly results that the modulation index contribute to the second order effect as a source to split the module trend for the two mismatch sources. The effect depends from the interaction between the EOL and EOM sidebands and the simulations clear effect induce a separation of the effects from the two different mismatch source to the module signal. This analysis was done to reduce this cross-talk effect and at the same time it was found that the modulation index reduction increases the lock stability.

In Figure 6.7 it is reported the measured effect. The left plot was obtained analysing the ration between the amplitude of the LG_{00} mode and the nearest EOM sidebands amplitude in acquisitions of the cavity scan for different F.P. values. The result on the left plot shows the dependence of the PDH slope from the DDS RF F.P. and consequently from the modulation index.
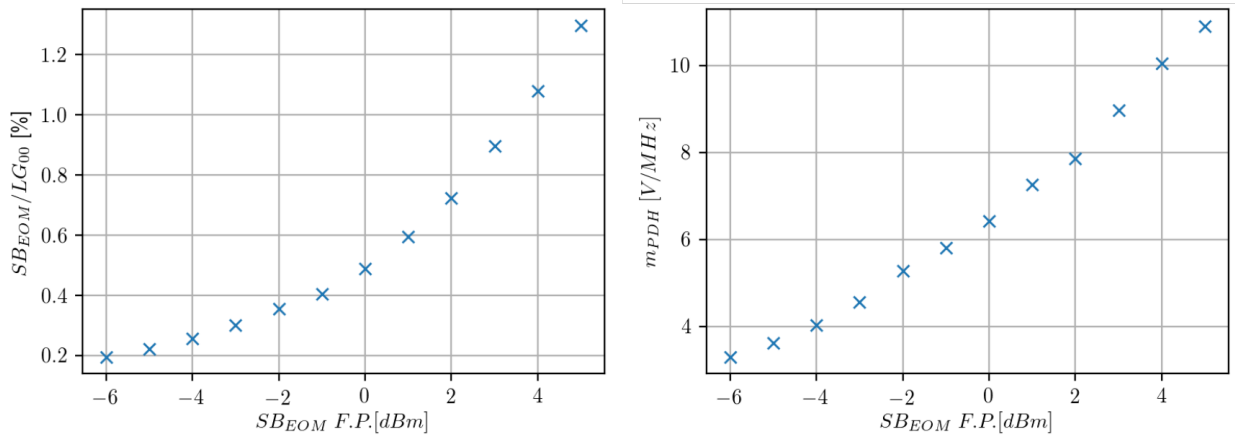
Figure 6.7: Studies of the EOM modulation index change with respect to the DDS RF F.P.
value (higher values equal to signals of higher Vpp). These measurements was done
analysing the peaks amplitude in cavity scan acquisitions. Left: EOM generated side-
band as a function of F.P., this plot can be considered as a calibration of the F.P. param-
eter in terms of the modulation index. Right: changes in the PDH slope in correspon-
dence of the $HG00$. A change of the PDH slope converts in a change in the error signal
FWHM.

After the confirmation that the EOM device can produce the required signals, it was studied how
the EOM modulation index (or modulation depth) changes the response of the feedback loop. In
Figure 6.8 are shown the results. For higher modulation index, the lock condition worsened, the
error signal FWHM increased and the mean transmitted amplitude reduced. For this analysis has
been considered measures with non perfect error signal mean value after the study of the I and Q
stability with non optimal laser frequency.

A complete characterization of the EOM modulation index effects requires a dedicated PID filter
parameter calibration for each index value. However, a stable PID filter configuration had already
been found. For this reason and to proceed with the final characterization and measurements, this
effect was considered as a perturbation. In addition, with the analysis of the error signal PSD
shows in Figure 6.9 the EOM modulation index has a similar effect to change the I.S. parameter.
 After all these considerations, the F. P. value was fixed to -5 dBm and the final value corresponding
modulation index is $\varepsilon^2 = (2.2231 \pm 0.0072) \cdot 10^{-3} [A.U.]$.

6.1.5 Ramp signal and FSR measurements

In this section are introduced the adopted procedures for the different signals calibrations. A dedi-
cated program for the Volt to frequency calibration of the error signal was developed in Python. In
order to obtain it, other two calibration were required. The method used, needed a first calibration
of the ramps signal used for the cavity scan procedure. The ramp signal slope is defined as the
ratio between the ramp Voltage and its time length. In the cavity scan process, this ramp is sent
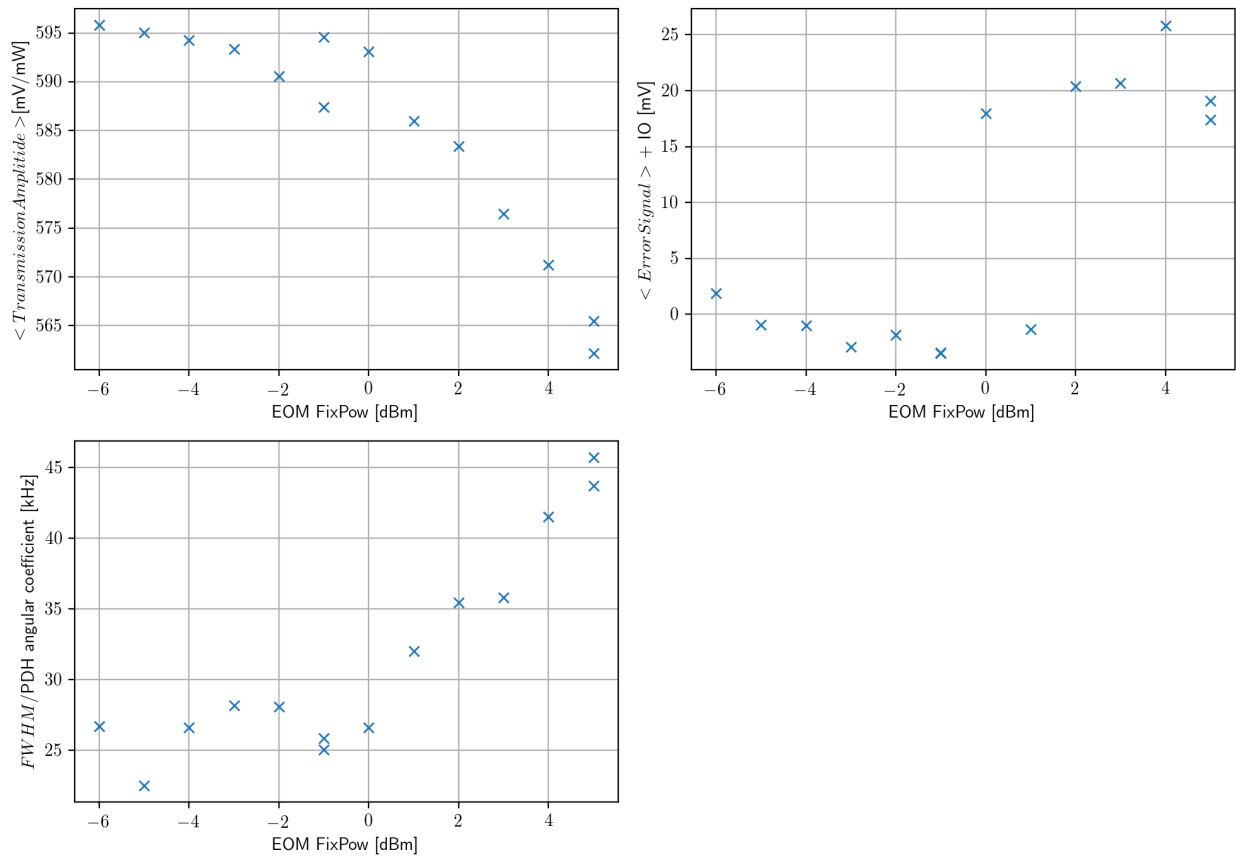
Figure 6.8: Study of the EOM index modulation. The experimental parameter that controls this index modulation is the DDS RF Fix Power (F.P.) (higher values equal to generation of higher Vpp signals). Top-Left: mean value of the transmitted power as a function of F.P., this plot shows that the transmitted amplitude reduces for higher values. Top-Right: estimated mean value of the error signal as a function of F.P., the introduction of the terms with higher error signal mean value are reintroduced afterwards. Bottom: study of the error signal FWHM, higher modulation index induce lock instabilities and higher FWHM values.
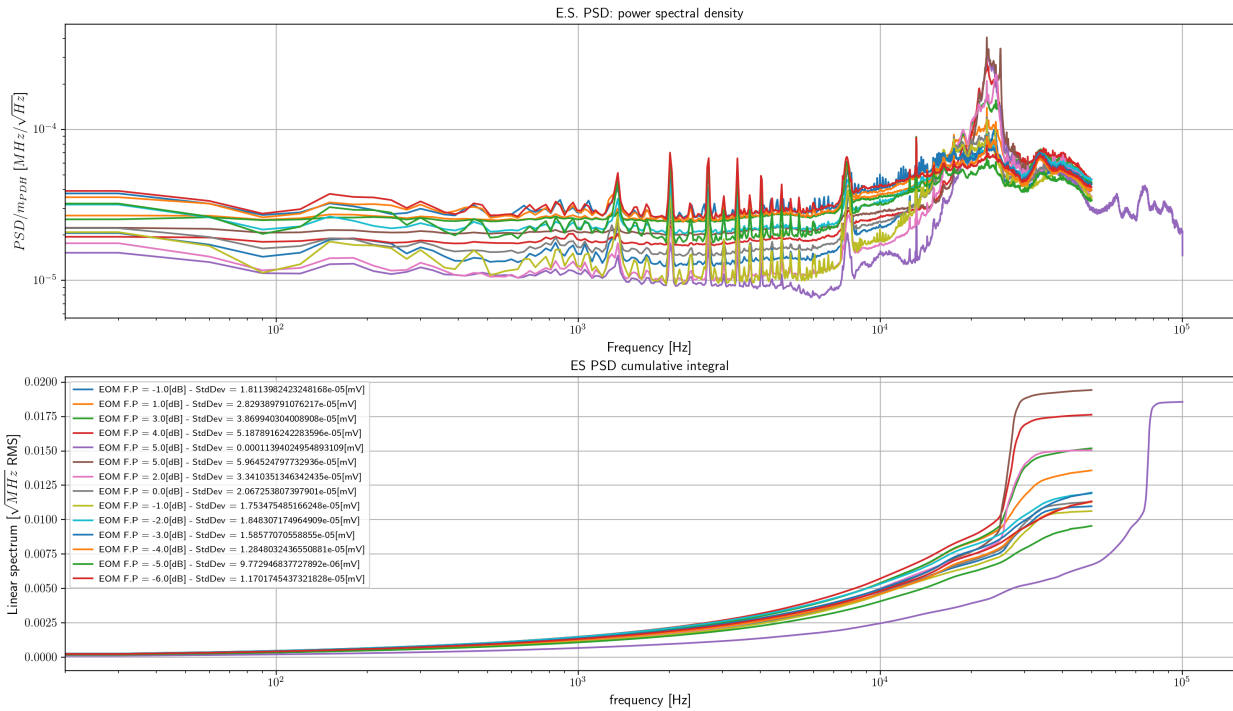
Figure 6.9: Scansion of the EOM index modulation changing the DDS RF F.P. value (higher values equal higher index modulations). This plot shows the Power Spectral Density of the error signal (PSD) and the RMS. Higher index modulations reduce low frequency fluctuations, but at the same time induces a resonance for higher frequencies and consequently a lock instability.

to the laser piezo to change the laser frequency in a proportional way with respect to this signal ramp. Consequently the time axis of the ramp signal and the one of the transmitted field acquired from the single-element are the same. For this reason it is possible to calibrate the time axis as a function of the ramp voltage.

The Moku:lab Data acquisition app does not permit to save its out ramp signal and in normal acquisation conditions both MMoku:lab inputs are used for the cavity scan acquisitions of the transmitted field and the PDH sognal. A different way was used to retrieve the information from the ramp directly from the PDH error signal. Analysing the cavity scansion acquisition, for a 10 Hz ramp, with amplitude of 440 mVpp, the error signal presents some discontinuities. Their distance coddesponds with the same ramp time length. Following this hint it was write a specific function to elaborate the error signal to retrieve the starting position of each ramp. With this method, it was possible to reconstruct the piezo response to the ramp signal. And it was verified with another acquisition that these discontinuities occur in correspondence with the ramp signal jumps

The analysis of the transmission signal for each single ramp required the development of a peak recognition filter. The filter was able to recognise the peaks and label them with their corresponding frequency HOM spacing (after a manual definition of the ramp length and the manual search of the fist discontinuity point for each cavity scan acquisition). From the analysis of the voltage distances of these peaks and their frequency distance it was possible to reconstruct a proper calibration and the piezo response to the ramp signal. The resultant calibration for the described setup
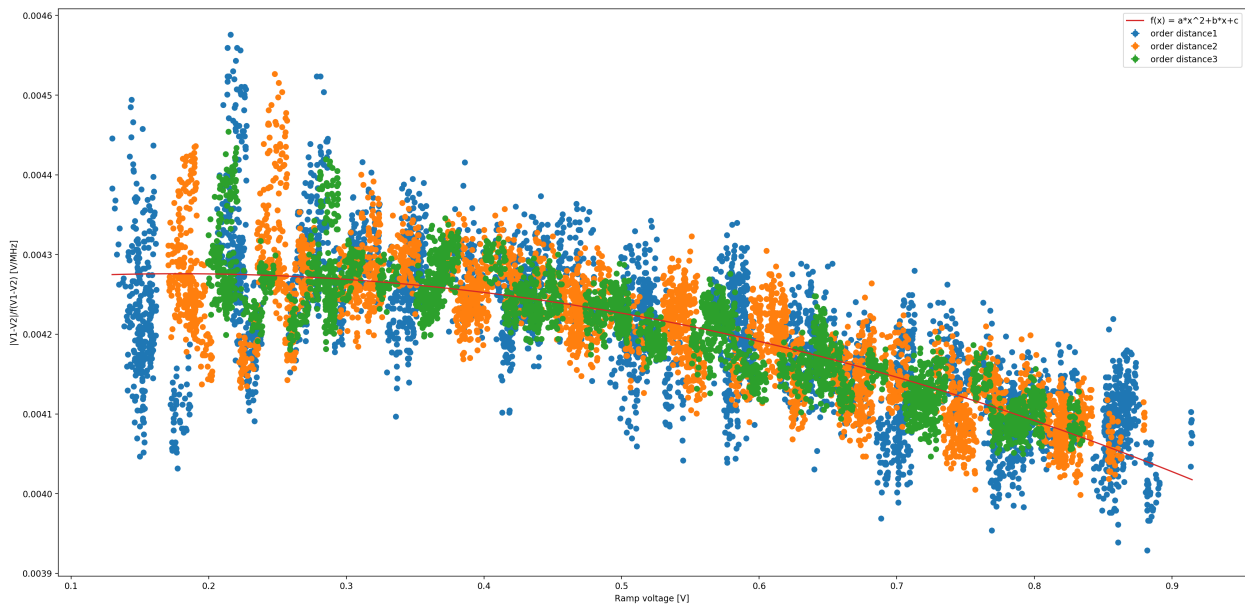
is reported in Figure 6.10

Figure 6.10: Frequency to ramp Voltage calibration. Here it is possible to observe the response of the piezo to the described ramp signal. The calibration was done by a second polynomial fit of the presented data. For the construction of this curve, the x-axis is set as the mean ramp voltage of two selected peaks and in the y-axis the ratio between the ramp voltage distances of the same two peaks and their frequency spacing. The order distance label used in this plot refers to the fact that only with maximum distance of 3 HOM spacing ere analysed.

In the next step, this new calibration is applied at the cavity scan acquisitions and permitting to characterize the higher order modes inside the FSR. In Figure 6.11 it is reported a calibrated FSR spectrum.

At the end, it was possible to define the final PDH calibration. A simple linear fit is used to fit the PDH signal near each LG_{00} frequency. The calibration parameter is the slope mean value obtained from the cavity scansion acquisitions.

6.2 EOL, optimization and measurements

Thanks to all the optimizations and characterizations done in the above sections, it is now possible to turn on the EOL device and start to characterize its effects. The first operation that was done inside the laboratory was to find the EOL optimal alignment to maximize the ON/OFF effect. The EOL positioning and initial characterization was already done in Nicolò Pisani's MSc thesis [6] but a fine positioning was still required. For this task was developed the peak finder algorithm described in the previous section. The other acquisitions done with EOL consists in the last acquired data for the characterization of the EOL modulation frequency and the test done for studying RF sensing technique.
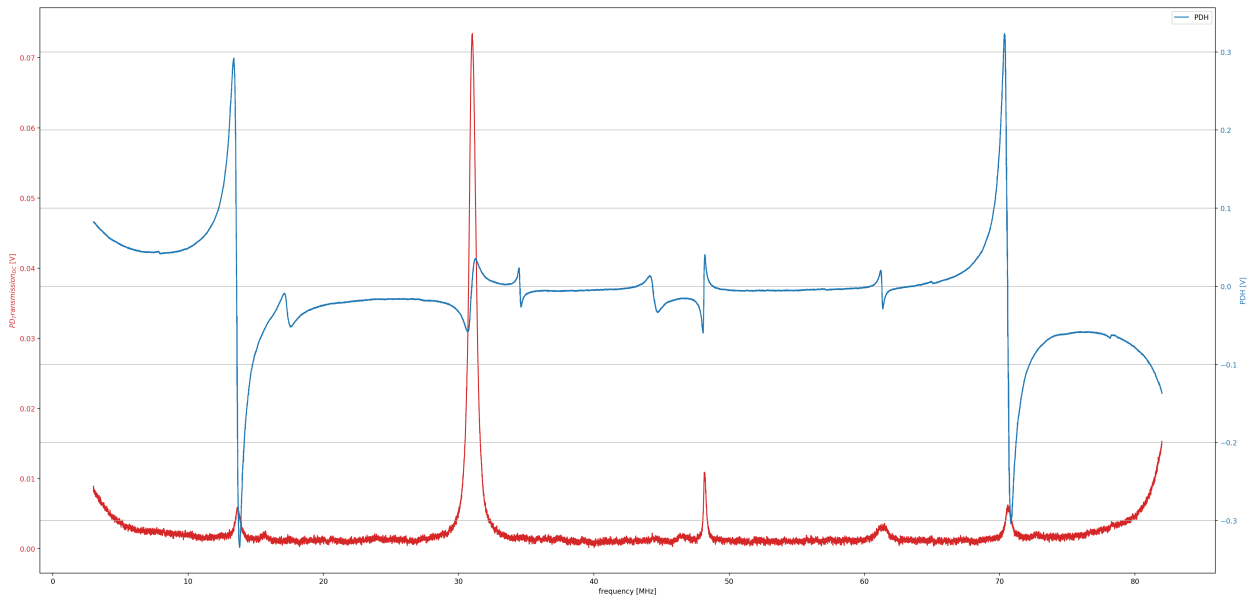
Figure 6.11: An acquisition of the cavity scansion. It is possible to observe both the transmission signal and the PDH error signal. From left: EOM positive sideband, LG_{10}, HG_{11}, the next peak was not recognised, probably a composition of different HOM, negative EOM sideband
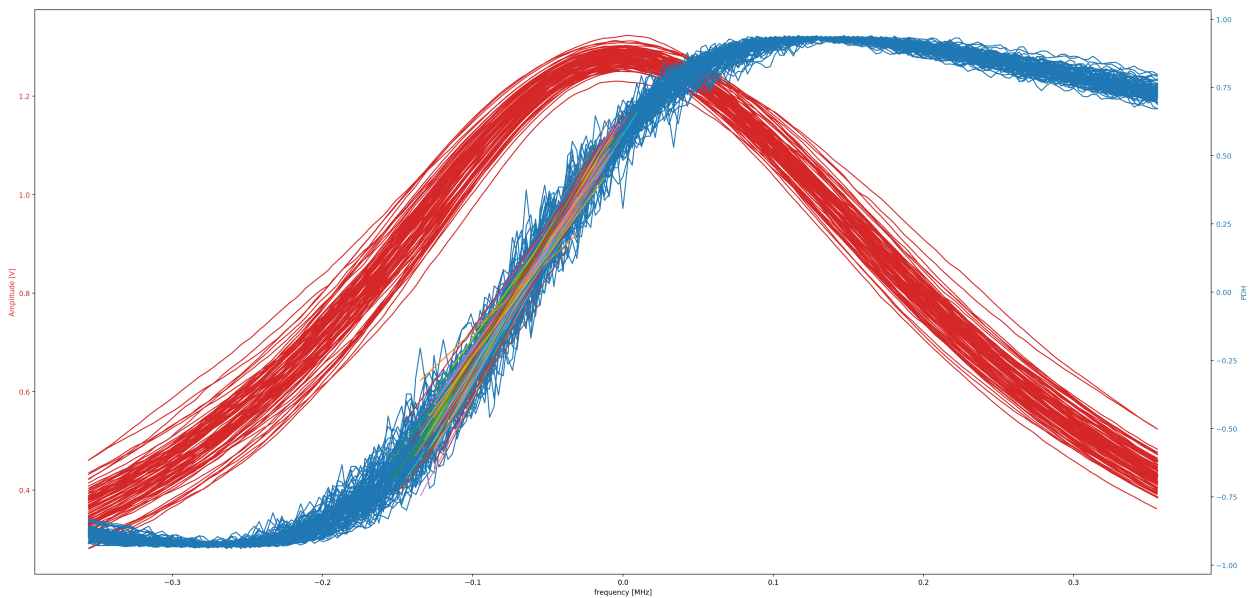

Figure 6.12: This plot is a superposition of all the LG_{00} peaks and PDH error signals of a cavity scansion acquisition. This figure shows how the error signal behaves with respect to the transmitted LG_{00} and the the selected part for the linear fit.

6.2.1 I/Q for varying lock offset

The first important test was the control on how the I and Q signals behave for a non perfect lock condition. The simulations described it as a necessary step in the to do list before the final acquisitions. The experimental measures were taken in two different ways: the first consists in acquiring the I and Q signal in the same condition of a cavity scansion. This method permits to obtain a complete frequency analysis for the I and Q signals. A not calibrated image in Figure 6.13 is presented in order to compare the signals behaviour with the simulated ones of Figure 4.2.
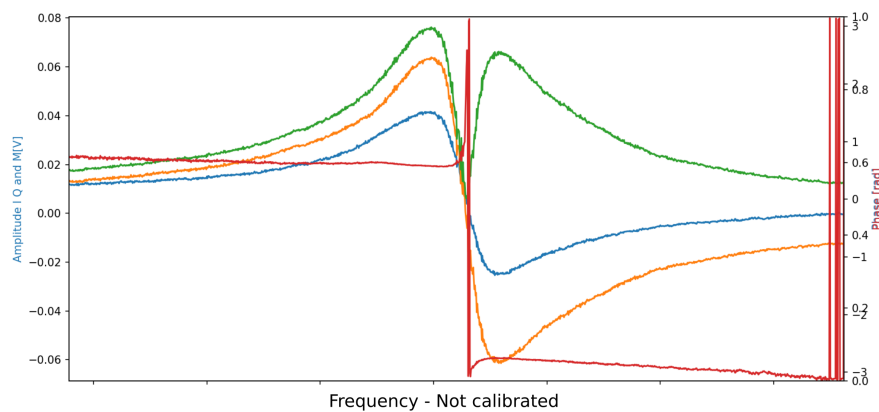

Figure 6.13: Preliminary image of the I (blue), Q (orange), Module (green) and Phase (red). This image was not calibrated, but thanks to another Moku:lab device it was possible to use the ramp trigger for both signals. A qualitative observation of both signal in the laboratory, confirms that the V shape of the module signal is near the transmitted LG_{00} mode and that the peak linewidth is comparable with these signals frequency range.

The second method consists in punctual acquisitions. This was done with lock conditions and the data was acquired for different IO values. The results of the second technique are reported here. These acquisitions covered an IO interval of [+20:-40] mV. For instance the cavity linewidth value is estimated to be: 687 ± 0.13. From the I and Q signals were subtracted their offset terms. their characterization were done with an acquisition of the I and Q signals in absence of the laser light. In Figure 6.14 are shown the experimental results. In conclusion, were reevaluated thanks to this analysis all the error signals acquisitions with difference from the error signal mean value and the IO lower than 20 mV. However, for the next sections,all the acquisitions were done with care to maintain a difference value lower that 10 mV.

6.2.2 I/Q for varying HOM value

In this section it is reported the last characterization before the final acquisitions. As it was presented, the theoretical description of this sensing technique requires a perfect match from the EOL modulation frequency and the LG_{01} mode frequency. From the cavity scansion calibration was
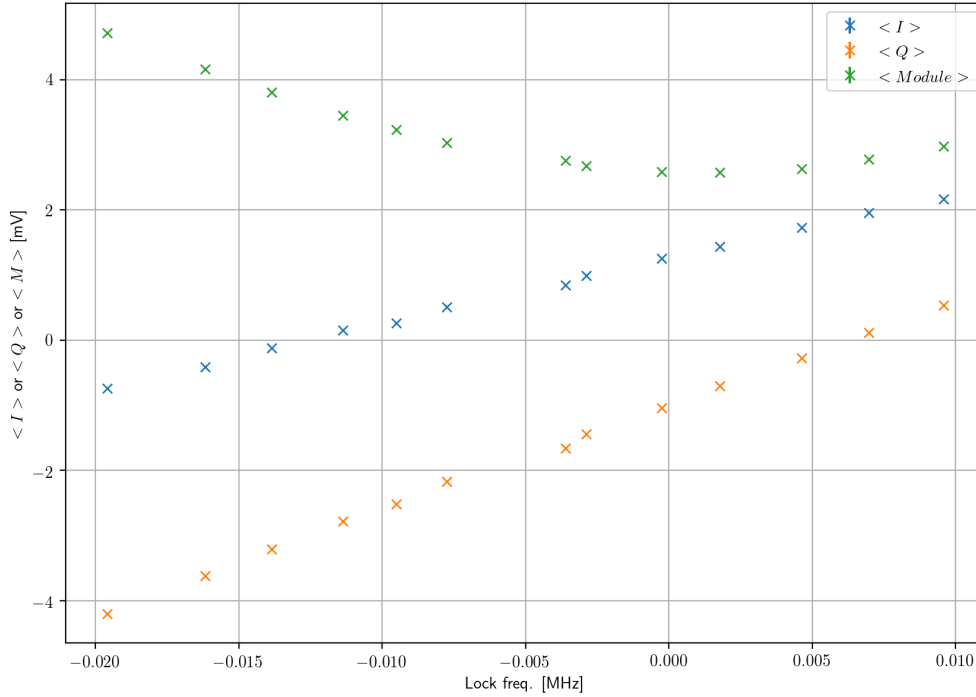
Figure 6.14: Trend of the I, Q and M signals in presence of a not correct laser lock frequency. The x-axis represents the difference from the two frequencies. This range is more than an order of magnitude smaller than the cavity linewidth.

retrived the LG_{01} frequency and it was extimated to be $\Omega = 30.94[MHz]$. This is the only situation where the simulation do not cover the experimental results and no explanation was actually found. It could be helpful to consider the residual phase modulation in the simulation.

6.2.3 I/Q for varying mode matching

In this last section the final results are presented. To test this RF sensing technique the telescope mounted after the EOL was used to generate different mismatch signals. The simulated cavity waist size required for a perfect match is $w_0 = 945.765 \ \mu m$ and a waist position of $z_0 = 2.7$ m from the beamsplitter placed before the EOM. It was decided to move only one of the two lenses in order to retrieve a mismatch signal that it is a composition of both the mismatch sources. The lenses can be translated thanks two micrometer translation stages and it was decided acquire data in all the possible range that the micrometer can cover. The mismatch values was simulated thanks to a Jammt simulation and was used for the x-axis of Figure 6.16. The presented mismatch is the squared value V_x that can be found in the Jammt cavity interface. At the I and Q signals was subtracted the same offset terms described in the previous section. Thanks to the offset subtraction, the I and Q signals now start from similar positions for lower mismatch signals. Both signals and module seems to present two trends each. The phase term is difficult to interpret because the I and Q signals present a residual constant phase term. The lens translation cover mismatch signals from 0.02% up to 10 % .
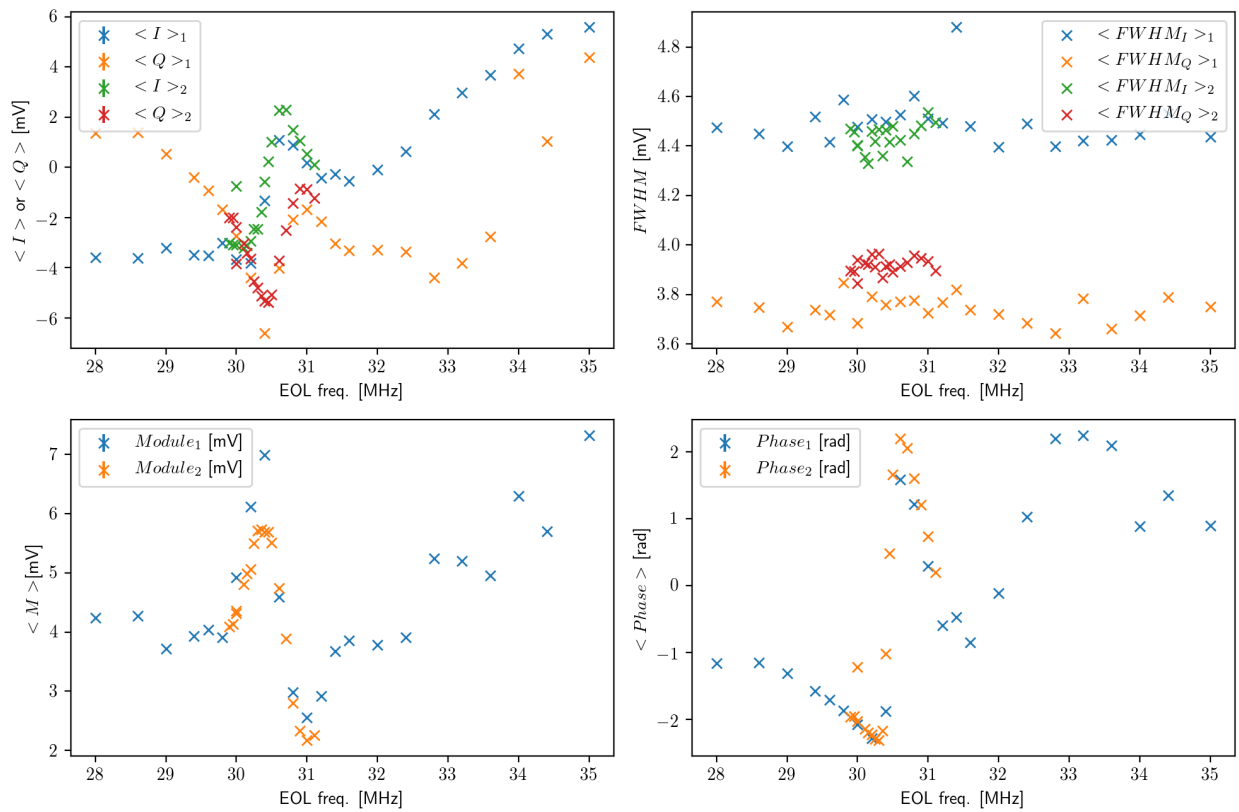
Figure 6.15: Experimental data of the I and Q error signals for different EOL modulating frequencies. Two series of acquisitions was done with different frequency steps. The first was done to scan the peak position and the second to help in finding the correct modulation frequency.
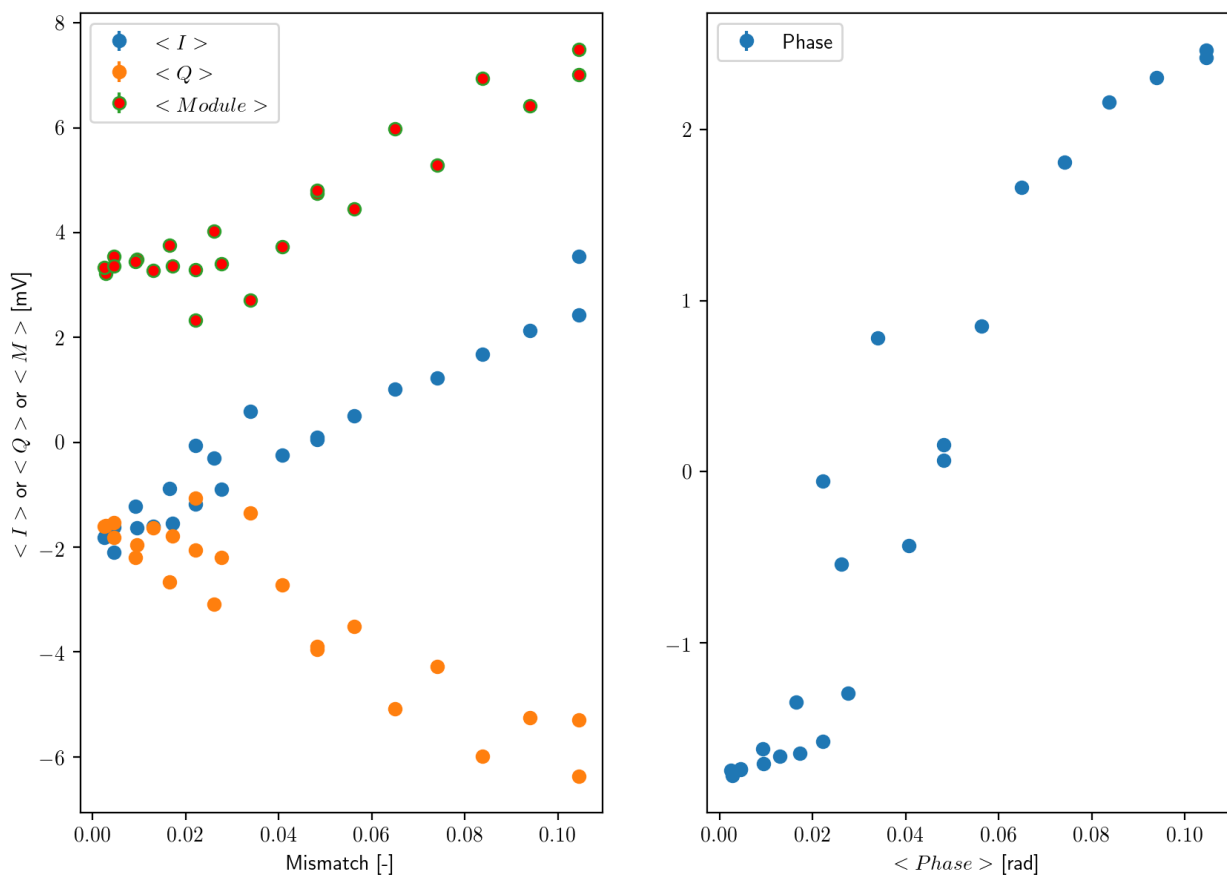
Figure 6.16: Experimental data of the I and Q error signals for different mismatch signals.The Module present a simil linear trend wiht respect to mismatch.

7 Conclusion

This thesis' aim was to demonstrate the RF sensing technique on a dedicated bench-top experiment employing an EOL prototype device. Starting from an already existing setup, parameters were optimized for the EOL alignment and working point, and for the cavity lock. To evaluate the system non-idealities were performed simulations and theoretical calculations of the cavity reflected field, considering Electro-Optic Modulator (for PDH technique), EOL modulations effects and interactions, including some system imperfections. Moreover an accurate study and optimization of the feedback loop parameters was done because the simulations confirm that this technique requires a stable cavity lock condition. Finally it was presented a characterization of the EOL error signal response to different mismatch conditions.

Bibliography

[1] B. E. Saleh and M. C. Teich, *Fundamentals of photonics*. john Wiley & sons, 2019.

[2] I. Kimel and L. R. Elias, "Relations between hermite and laguerre gaussian modes," *IEEE Journal of quantum electronics*, vol. 29, no. 9, pp. 2562–2567, 1993.

[3] N. Hodgson and H. Weber, *Laser Resonators and Beam Propagation: Fundamentals, Advanced Concepts, Applications*, vol. 108. Springer, 2005.

[4] N. Ismail, C. C. Kores, D. Geskus, and M. Pollnau, "Fabry-pérot resonator: spectral line shapes, generic and related airy distributions, linewidths, finesses, and performance at low or frequency-dependent reflectivity," *Optics express*, vol. 24, no. 15, pp. 16366–16389, 2016.

[5] A. E. Siegman, "Lasers university science books," *Mill Valley, CA*, vol. 37, no. 208, p. 169, 1986.

[6] N. Pisani, "Sviluppo di una lente elettro-ottica per misure di accoppiamento laser in cavitã a radiofrequenza," 2018.

[7] T. Skettrup, T. Meelby, K. Færch, S. L. Frederiksen, and C. Pedersen, "Triangular laser resonators with astigmatic compensation," *Applied optics*, vol. 39, no. 24, pp. 4306–4312, 2000.

[8] F. Raab and S. Whitcomb, "Estimation of special optical properties of a triangular ring cavity," *LIGO-T920004*, 1992.

[9] H. Wang, M. Dovale-Álvarez, C. Collins, D. D. Brown, M. Wang, C. M. Mow-Lowry, S. Han, and A. Freise, "Feasibility of near-unstable cavities for future gravitational wave detectors," *Physical Review D*, vol. 97, no. 2, p. 022001, 2018.

[10] D. Z. Anderson, "Alignment of resonant optical cavities," *Applied Optics*, vol. 23, no. 17, pp. 2944–2949, 1984.

[11] M. Granata, C. Buy, R. Ward, and M. Barsuglia, "Higher-order laguerre-gauss mode generation and interferometry for gravitational wave detectors," *Physical review letters*, vol. 105, no. 23, p. 231102, 2010.

[12] P. Fulda, D. Voss, C. Mueller, L. Ortega, G. Ciani, G. Mueller, and D. Tanner, "Alignment sensing for optical cavities using radio-frequency jitter modulation," *Applied Optics*, vol. 56, no. 13, pp. 3879–3888, 2017.

[13] R. Weis and T. Gaylord, "Lithium niobate: summary of physical properties and crystal structure," *Applied Physics A*, vol. 37, no. 4, pp. 191–203, 1985.

[14] A. Yariv and P. Yeh, *Optical waves in crystals*, vol. 5. Wiley New York, 1984.

[15] J. Frejlich, *Photorefractive materials: fundamental concepts, holographic recording and materials characterization*. John Wiley & Sons, 2007.

[16] J. I. Thorpe, K. Numata, and J. Livas, "Laser frequency stabilization and control through offset sideband locking to optical cavities," *Optics express*, vol. 16, no. 20, pp. 15980–15990, 2008.

[17] F. Bondu and O. Debieu, "Accurate measurement method of fabry-perot cavity parameters via optical transfer function," *Applied optics*, vol. 46, no. 14, pp. 2611–2614, 2007.

[18] H. Shen, L. Li, J. Bi, J. Wang, and L. Chen, "Systematic and quantitative analysis of residual amplitude modulation in pound-drever-hall frequency stabilization," *Physical Review A*, vol. 92, no. 6, p. 063809, 2015.

[19] A. M. Thomas, "Mode mismatch detection using an electro-optic lens device." `http://www.phys.ufl.edu/ireu/IREU2019/pdf_reports/Ann_Mariam_Thomas_Report_final_IREU_Padova.pdf`, 2019.

[20] "Moku:lab pid controller datasheet." https://liquidinstruments.com/pid-controller/, 2019.

[21] X. Shi, J. Zhang, X. Zeng, X. Lü, K. Liu, J. Xi, Y. Ye, and Z. Lu, "Suppression of residual amplitude modulation effects in pound–drever–hall locking," *Applied Physics B*, vol. 124, no. 8, p. 153, 2018.